INDUCED POLARIZATION EFFECT IN TIME DOMAIN: THEORY, MODELING, AND APPLICATIONS

by

Lei Fu

A thesis submitted to the faculty of
The University of Utah
in partial fulfillment of the requirements for the degree of

Master of Science

in

Geophysics

Department of Geology and Geophysics

The University of Utah

December 2011

The University of Utah Graduate School

STATEMENT OF THESIS APPROVAL

The thesis of **Lei Fu**

has been approved by the following supervisory committee members:

Michael S. Zhdanov	, Chair	**10/07/2011** Date Approved
Vladimir Burtman	, Member	**10/07/201** Date Approved
Erich U. Petersen	, Member	**10/24/201** Date Approved

and by **D. Kip Solomon** , Chair of the Department of **Geology and Geophysics**

and by Charles A. Wight, Dean of The Graduate School.

ABSTRACT

A new theoretical and experimental method of induced polarization (IP) in the time domain is tested with resistivity data and detailed mineralogy of rock samples. The Generalized Effective Medium Theory of Induced Polarization (GEMTIP) was originally developed in the frequency domain for explaining the structure-property relationship of rocks. The geoelectrical parameters of this model are determined by the intrinsic petrophysical and geometric characteristics of composite media: the mineralization and/or fluid content of rocks and the matrix composition, porosity, anisotropy, and polarizability of formations. The physical properties of rock samples from exploration or mining sites are often used to assist in planning geological surveys or interpretation of geophysical results. However, electrical property data are often recorded in the time domain. In this paper, the Generalized Effective Medium Theory of Induced Polarization (GEMTIP) is tested with the time domain resistivity data transformed from complex resistivity data. It is demonstrated that the time-domain GEMTIP method can be used to study the induced polarization (IP) effect. Results indicate that the time domain resistivity data from laboratory measurements can be used in inversion routines. With advances in the understanding of the IP effect through the GEMTIP model and wide application of the time domain measurements, detection, and discrimination capability will improve for porphyry systems and other geologic targets, leading to greater efficiency in mineral exploration.

CONTENTS

CHAPTER 1

PRINCIPLES AND APPLICATION OF THE INDUCED POLARIZATION EFFECT

1.1 Introduction

The electromagnetic (EM) data observed in geophysical experiments generally reflect two phenomena: (1) electromagnetic induction (EMI) in the earth and (2) the induced polarization (IP) effect related to the relaxation of polarized charges in rock formations. The induced polarization (IP) method was first observed by Conrad Schlumberger in France (1913). The theoretical and experimental foundations of IP methods were continued by A. S. Semenov, Y. P. Bulashevich, S. M. Sheinman, V. A. Komarov, T. Madden, H. Seigel, J. Wait, S. Ward, J. Hohmann, K. Zonge, and many others (see review by Seigel et al., 2007).

Practical use of the IP method can be traced to the 1950s, when mining and petroleum companies actively looked into application of this method to mineral exploration. The physical-mathematical principles of the IP effect were originally formulated in pioneering works by Wait (1959) and Sheinman (1969). However, this method was not widely used in U.S. industry until after the work of Zonge and his associates at the Zonge Engineering and Research Organization (Zonge, 1974; Zonge and Wynn, 1975) and by Pelton (1977) and Pelton et al. (1978) at the University of Utah. Significant contribution to the development of the IP method was also made by Wait (1959, 1982) and by the research team at Kennecott from 1965 through 1977 (Nelson, 1997). IP surveys can be more sensitive to mineralization, pore fluids, and other rock parameters compared to DC resistivity surveys. There are several models developed to describe the IP effect. The well-accepted empirical model, the Cole-Cole model (Cole and Cole, 1941), was first adopted by Pelton (Pelton, 1978). The Generalized Effective Medium Theory of Induced Polarization (GEMTIP) was developed by Zhdanov in 2006, and is tested in the following chapters.

1.2 The Induced Polarization Effect

The IP effect is thought to be caused by electrochemical reactions and charge build up at interfaces, grain boundaries, vein walls and other boundaries (Frasier, 1964). The IP effect of a disseminated mineralization and a mineralized vein is shown in Figure 1.1. Current is applied across a host rock with metallic mineral inclusions. The porous region around the metallic inclusion is generally saturated with fluid, allowing ions to travel across. The metallic inclusions become polarized, and attract positive ions to form an electrical double layer at the boundary of the inclusions. This causes charge build up to occur, thus impeding current flow. As a result, when the current is abruptly terminated, instead of immediately dropping to zero, the voltage gradually decays.

1.3 Cole-Cole Model

The Cole-Cole model (Kenneth S. Cole and Robert H. Cole, 1941), demonstrated by Pelton (Pelton et al., 1978), is an excellent representation of the complex resistivity (real and imaginary) of polarized rock formations. This frequency-dependent complex resistivity is illustrated in Figure 1.2, which is described in the following formula:

$$\rho(\omega) = \rho_{DC}\left(1 - m\left(1 - \frac{1}{1 + (-i\omega\tau)^{\mathrm{C}}}\right)\right) \tag{1.1}$$

where ρ_{DC} is the dc resistivity (Ohm-m); ω is the angular frequency (rad/sec); the time constant, τ, determines at what frequency the peak response in the imaginary resistivity will occur, whereas the dimensionless intrinsic chargeability, m, characterizes the intensity of the IP effect and the relaxation parameter, C, depicts its magnitude. These effects can been seen graphically in Figure 1.2 (Emond, 2007).

Characterizing observed IP responses in terms of their Cole-Cole parameters has proven useful in resolving different rocks, but primarily through differences in their average particle size. Grounded metallic structures have been easily recognized by the long time constant of their IP responses. However, despite much effort, attempts to predict the mineralogical composition of rocks by analysis of IP response characteristics have not been very fruitful (Seigel et al.).

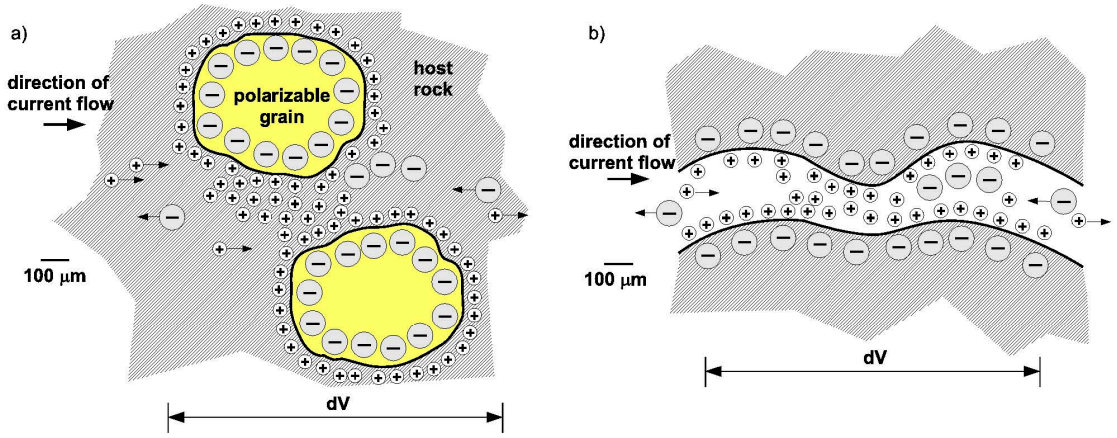

modified from Frazier 1964

Figure 1.1. Conceptual illustrations of surface polarization. a) Surface polarization of disseminated minerals in a uniformly conductive host rock. b) Surface polarization of a mineralized vein.

The resistivity behavior of the Cole-Cole model transformed in the time domain by changing different parameters is shown in Figure 1.3. The resistivity increases with time. The IP effect happens in later time when increasing the time constant (τ). The difference between the amplitude of the IP effect at early time and that at later time is greater by increasing chargeability (m). Also a larger value of relaxation parameter (C) leads to steeper resistivity curve against time.

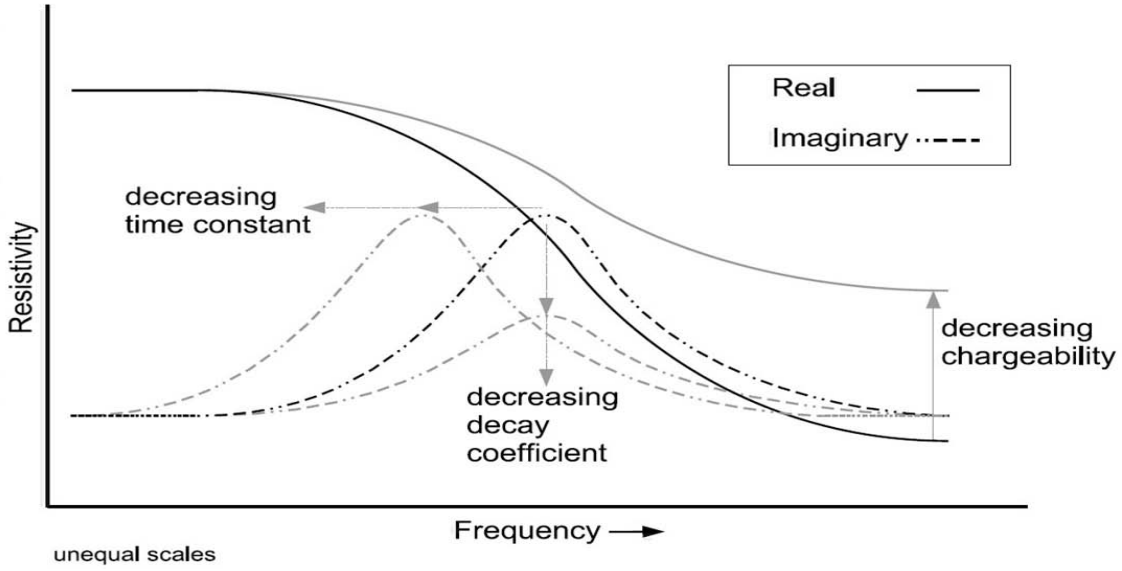

Figure 1.2. Complex resistivity behavior of the Cole-Cole model in the frequency domain. The effect of charging chargeability (m), time constant (τ), and decay coefficient (C) from the formula is illustrated (Emond, 2007).

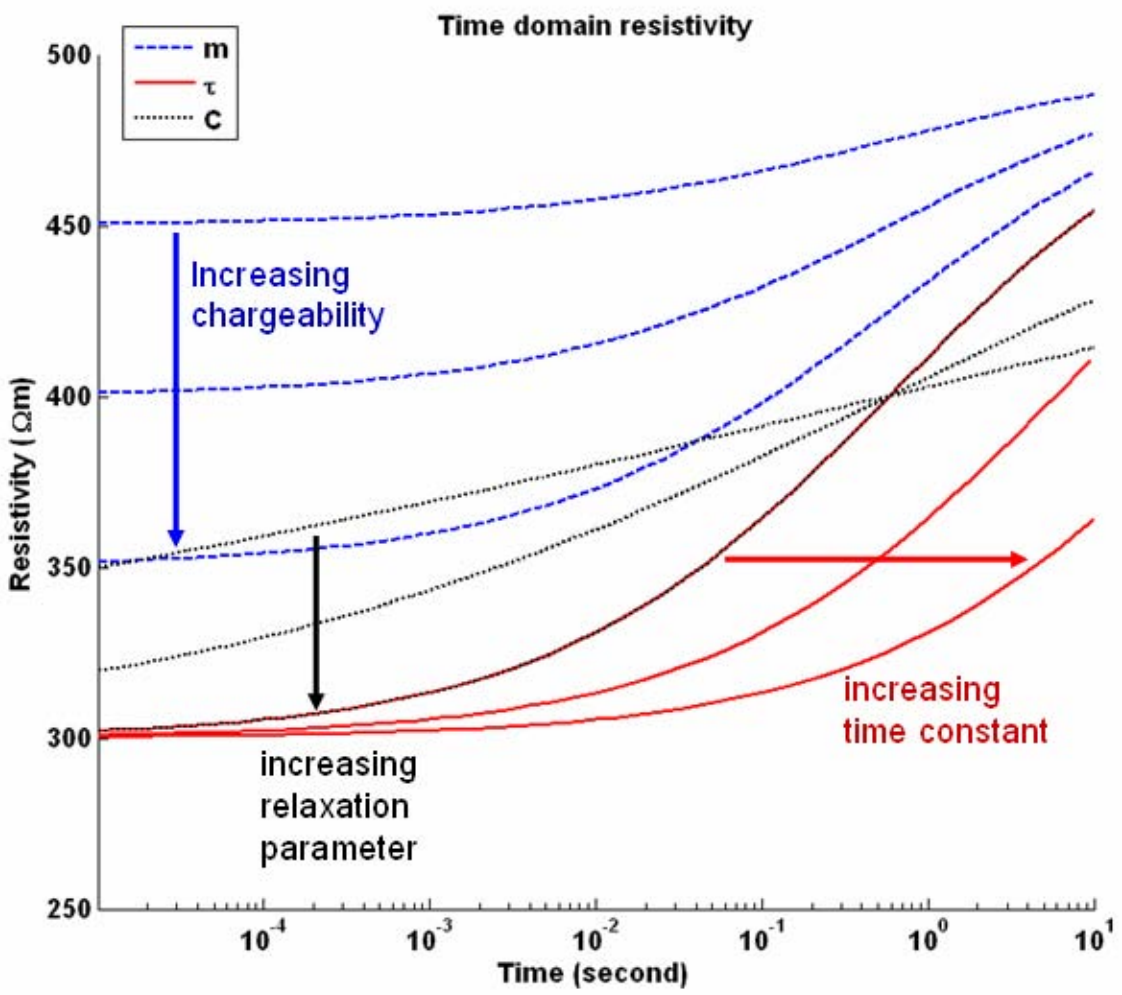

Figure 1.3. The behavior of the Cole-Cole model transformed in the time domain. The effect of changing chargeability (m), time constant (τ), and decay coefficient (C) from the formula is illustrated.

CHAPTER 2

IP EFFECT IN THE FREQUENCY DOMAIN

2.1 Frequency-domain IP

Conrad Schlumberger was the first to describe conclusively an IP phenomenon in his monograph, published in 1920.

In the three decades that followed, there were no further significant developments in this field until Brant and his group's work at Newmont Exploration Limited in 1946, which later sparked an application report by Bleil (1953) and a comprehensive series of articles under the guidance of MIT Professor Madden (1957-1959). Bleil's (1953) pulse IP equipment was conceived during World War II and the equipment of Vacquier et al. (1957) was similar to Newmont's. The first commercial pulse IP equipment was marketed by Hunting in 1957 and was followed by that of Seigel and associates in 1958.

Madden and his coworkers did a variety of basic theoretical and laboratory research studies with emphasis on IP effects due to nonmetallic causes. They used their frequency IP equipment in the field survey in Nova Scotia in 1955 (Madden and Marshall, 1958). Advantages in the frequency-domain IP equipment design inspired McPhar in 1957, Geoscience, Inc in 1959, and Heinrichs Geoexploratoin Co. in 1960 to develop their own apparatuses. Mining companies, including Kennecott and Phelps Dodge, produced similar frequency-domain instruments, while ASARCO adhered to the pulse equipment. Anacondas geophysical division under McAlister perfected phase-sensitive field equipment in 1955.

Research on induced polarization in the Soviet Union started in 1941, according to Dakhnov's descriptions of this method in petroleum well logging.

In the years between 1955 and 1960, several universities, mining companies, and government agencies are involved in the IP research because of the success of the method in exploring for metallic minerals. Researchers at the University

of California at Berkeley, Michigan Technological University, Missouri School of Mines, the University of Utah, and the U.S. Geological Survey were engaged in IP research in the 1960s and 1970s. Some base-metal mining companies, including Kennecott Copper, Anaconda, American Smelting and Refining Co., and Phelps Dodge, started their own research on IP.

In 1960, Newmont Exploration Limited supported a program for IP instrument design with Varian Associates of Palo Alto, California, for the development of low-frequency, phase-sensitive, frequency-domain equipment.

Dolan and McLaughlin (1967) summarized previous frequency-domain work and also their time-domain IP instrument development.

Various characteristics of the IP decay curves have been studied by different groups, but there are not many general statistical compilations of the basic phenomenon beyond observing that to a first approximation the decay curve is logarithmic and the IP phenomenon is linear. Dolan and McLaughlin found that the normalized shape of the decay curve for 575 laboratory sample measurements varies between the rather close limits. It is interesting to see that it is possible to define a normalized standard decay curve with a fairly consistent logarithmic shape and a decay constant in the 0.1-1.0 s. Hohmann et al. (1970) and other investigators have documented these characteristics in the frequency and phase domains.

K. L. Zonge and his associates in Tucson, Arizona, have designed a completely digitized filled IP unit, which uses a digital computer to direct operations and analyze results. Zonges IP transmitter sends out a series of square-wave current signals which are sampled by the digital computer and then compared in real time with the exact amplitude of the in-phase and out-of-phase voltage responses. The harmonic frequencies of the square waves are used in the analysis technique. The field data thus consist of the complete IP response spectrum with both real and imaginary components.

The frequency effect (FE) is determined from data of two different frequencies generally a decade apart (Zonge et al., 1972). Because differences in subsurface geology cause different perturbations in the observed data, FE can be useful for interpretation of IP data. The frequency effect is defined as:

$$FE = \frac{V_2 - V_1}{V_1} \tag{2.1}$$

or in term of resistivity,

$$FE = \frac{\rho_2 - \rho_1}{\rho_1} \tag{2.2}$$

The simplest form of FE compares the recorded voltages at two frequencies and is given by equation 2.1. It can be transformed into equation 2.2 by using the calculated apparent resistivity values, ρ_2 and ρ_1. Percent FE is calculated multiplying FE by 100 (Zonge et al., 1972).

The above interpretation techniques proved useful for obtaining geologic information in exploration.

A resistivity spectrum is a display of rock resistivity as a function of frequency. To contrast such a diagram, the resistivity or voltage level is assigned 100% at the datum frequency. Resistivities at other frequencies over spectral range are normalized relative to the datum. The resistivity spectrum of a rock is concave down at the low-frequency end of the Warburg impedance and convex down at the high-frequency end. This relationship was noted by Fraser et al. (1964), who then pointed out that massively mineralized rocks should have convex-down spectral curves. Disseminated mineralized or membrane polarization rock with higher resistivity should ideally display concave-down spectral curves.

2.2 Frequency-domain GEMTIP

The analysis of IP phenomena is usually based on models with frequency-dependent complex conductivity distribution. As we discussed above, one of the most popular is the Cole-Cole relaxation model and its different modifications (Cole and Cole, 1941). The parameters of the conductivity-relaxation model can be used for discrimination of different types of rock formations, an important goal in mineral exploration. Until recently, these parameters have been determined mostly in the physical laboratory by direct analysis of samples.

Zhdanov (2006) introduced a new composite geoelectric model of rock formations based on the effective-medium approach that generates a conductivity model with parameters directly related by analytic expressions to the physical characteristics of the microstructure of rocks and minerals (microgeometry and

conductivity parameters). This composite geoelectric model provides more realistic representation of complex rock formations than conventional unimodal-conductivity models, which permits modeling the relationships between the geometric factors and physical characteristics of different types of rocks (e.g., grain size, shape, conductivity, polarizability, fraction volume, and so forth) and the parameters of the relaxation model.

Effective-medium approximation for composite media has been discussed in many publications. The general formalism of the effective-medium theory (EMT) was developed by Stroud (1975). The advances of physical EMTs (e.g., Landauer, 1978; Norris et al., 1985; Shwartz, 1994; Sihvola, 2000; Kolundzija and Djordjevic, 2002; Berryman, 2006) make it possible to develop a rigorous mathematical model of multiphase heterogeneous conductive media excited by an EM field. The EMT and its different extensions were applied successfully to the study of macroscopically isotropic and anisotropic models of rock formations in electrical geophysics (e.g., Sen et al., 1981; Mendelson and Cohen, 1982; Sheng, 1991; Kazatchenko et al., 2004; Toumelin and Torres-Verdn, 2007, and so forth).

The existing form of EMT and its modifications, however, do not allow the inclusion of the induced-polarizability effect in the general model of heterogeneous rocks. The conventional EMT models describe the electromagnetic-induction effect caused by electrical heterogeneity of the multiphase medium, whereas the IP effect is manifested by additional surface polarization of the grains caused by the complex electrochemical reactions that accompany current flow within the formation.

It is well known, however, that the effective conductivity of rocks is not necessarily a constant and real number but can vary with frequency and be complex (Shuev and Johnson, 1973). There are several explanations for these properties of effective conductivity. Most often, they are explained by physical-chemical polarization effects of mineralized particles of rock material and/or by electrokinetic effects in the pores of reservoirs (Wait, 1959; Marshall and Madden, 1959; Luo and Zhang, 1998). Thus, polarizability is caused by the complex electrochemical reactions that accompany current flow in the earth. These reactions occur in a heterogeneous medium representing rock formations in areas of mineralization and hydrocarbon reservoirs. This phenomenon is usually explained as a surface polarization of mineralized particles and the surface of a moisture-porous space that occurs under

the influence of an external electromagnetic field. It is manifested by accumulating electric charges on the surface of different grains forming the rock. This effect is significant in the case of a metal-electrolyte interface (Bockrih and Reddy, 1973). However, a similar effect is observed at the interface between electrolyte and typical rock-forming minerals such as silicate and carbonate (Komarov, 1980).

Zhdanov (2006) demonstrated that EMT formalism can be used in the theory of formation polarizability as well. A generalization of the classical EMT approach consists of two major parts: (1) introduction of the effective-conductivity models of the heterogeneous, multiphase rock formations with inclusions of arbitrary shape and conductivity by using the principles of the Born-type quasi-linear (QL) approximation in the framework of EMT formalism; (2) development of the generalized effective-medium theory of induced polarization (GEMTIP), which takes into account electromagnetic induction (EMI) and induced polarization (IP) effects related to the relaxation of polarized charges in rock formations.

The general model applies to mineralization zones and hydrocarbon reservoirs. It develops a unified physical-mathematical model to examine EM effects in complex rock formations that accounts for mineral composition, electrical properties, fluid content, matrix composition, porosity, anisotropy, and polarizability. It provides a link between the volume content of different minerals and/or the hydrocarbon saturations and the observed EM field data.

CHAPTER 3

IP EFFECT IN THE TIME DOMAIN

3.1 Time-domain IP

There are several different ways of measuring the IP effect in the time domain. One measure is the area between the decay curve and the zero volt level. The pulsed constant-current time-domain input waveform and typical voltage response waveform over mineralized or polarizable ground are shown in Figure 3.1. This value is usually normalized by dividing it by the peak charging voltage.

The labeled portions of the waveform are used in defining the theoretical definition. The unitless parameter m, derived by Seigel (1959) and often called the theoretical chargeability, is defined as:

$$m = \frac{V_s}{V_p} \tag{3.1}$$

Chargeability in the time domain refers to the discharge of the polarizable media and can be defined in two methods. This method is the ratio of the secondary voltage (V_s) to the primary voltage (V_p) shown in Equation 3.1 and illustrated in Figure 3.1 (Sumner, 1976). When the inducing current is turned off, the primary voltage almost immediately drops to a secondary response level and then the transient decay voltage diminishes with time. The second method integrates the decaying secondary voltage (V_t) over the time interval t_1 to t_2 and divides by the primary voltage (V_p) expressed in equation 3.2 (Sumner, 1976).

$$M = \frac{1}{V_p} \int_{t_1}^{t_2} V_t \, \mathrm{d}t \tag{3.2}$$

where t_1 and t_2 define a time interval on the discharge curve which excludes major voltage transients due to electromagnetic coupling effects.

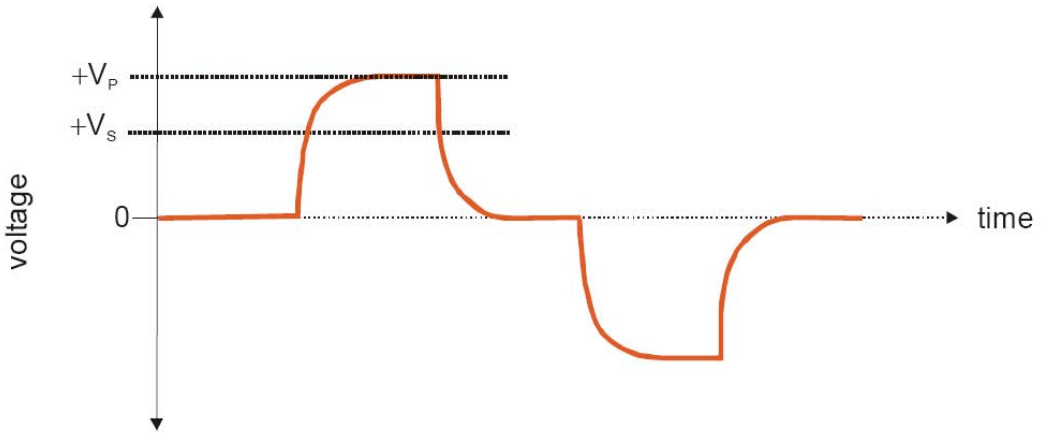

Figure 3.1. The IP pulse or time-method waveforms, ideally due to a long-period pulse, showing the induced primary current being detected as a maximum primary voltage V_p. When current is turned off, voltage drops to a secondary level V_s and the transient voltage decays with time (Modified from Summer, 1976).

3.2 Time-domain GEMTIP

The generalized effective-medium theory of induced polarization (GEMTIP) considers a composite geoelectrical model of rock formations using the effective-medium approach, which generates a conductivity model with parameters directly related by analytical expressions to the physical characteristics of the microstructure of rocks and minerals (Zhdanov, 2008). As a result, GEMTIP can be used to produce complex resistivity (CR) spectra of mineral rocks in the frequency domain. GEMTIP combines the rigors of Maxwells equations at low frequency with IP relaxation mechanisms.

Following the principles of the GEMTIP approach, we represent a complex heterogeneous rock formation as a composite model formed by a homogeneous host medium of a volume V with a (complex) conductivity tensor $\hat{\sigma}_0(r)$ (where r is an observation point) filled with grains of arbitrary shape and conductivity. The rock is composed of a set of N different types of grains, the lth grain type having (complex) tensor conductivity $\hat{\sigma}_l(r)$. The grains of the lth type have a volume fraction fl in the medium and a particular shape and orientation. The polarizability effect is usually associated with surface polarization of the coatings of the grains. This surface polarization can be related to electrochemical charge transfer between the grains and a host medium (Wong, 1979; Wong and Strangway,

1981; Klein et al., 1984). The surface polarization is manifested by accumulating electric charges on the surface of the grain. A double layer of charges is created on the grain's surface, which results in the voltage drop at this surface (Wait, 1982). The polarizability effect is quantitatively represented in the fundamental equations of the GEMTIP model through the volume depolarization tensor, $\hat{\Gamma}_l$, and a surface polarizability tensor $\hat{p}$ (Zhdanov, 2008). A general solution of the effective conductivity problem for an arbitrary multiphase composite polarized medium is provided by the following expression:

$$\hat{\sigma}_e = \hat{\sigma}_0 + \sum_{l=1}^{N} [\hat{I} + \hat{p}_l]^{-1} [\hat{I} - \Delta\hat{\sigma}_l^p \hat{\Gamma}_l]^{-1} [\hat{I} + \hat{p}_l] \Delta\hat{\sigma}_l f_l \tag{3.3}$$

where $\Delta\hat{\sigma}_l = \hat{\sigma}_l - \hat{\sigma}_0$ is anomalous conductivity, and $\hat{\sigma}_l^p$ is a "polarized" anomalous conductivity:

$$\hat{\sigma}^p(r) = [\hat{I} + \hat{p}(r)] \Delta\hat{\sigma}(r) \tag{3.4}$$

This formula allows us to find the effective conductivity for inclusions with arbitrary shape and electrical properties. That is why the composite goelectrical model of the IP effect may be used to construct the effective conductivity for realistic rock formations typical for mineralization zones and/or petroleum reservoirs. In the case of an isotropic multiphase composite model, with all model parameters described by the scalar functions, equation 3.3 can be simplified. For example, if a composite model is formed by a homogeneous host medium of a volume V with a conductivity σ_0 filled with grains of spherical shape, and we assume that we have a set of N different types of grains, the lth grain type having radius a_l, conductivity σ_l, and surface polarizability k_l, the volume depolarization tensors are constant scalar tensors equal to (Zhdanov, 2008):

$$\hat{\Gamma}_l = \Gamma_l \hat{I} = -\frac{1}{3\sigma_b} \hat{I} \tag{3.5}$$

The surface polarizability tensor $\hat{p}_l$ also becomes a scalar tensor and equals to:

$$\hat{p}_l = p_l \hat{I} = 2k_l a_l^{-1} \sigma_b \sigma_l (\Delta\sigma_l)^{-1} \hat{I} \tag{3.6}$$

In the last formula, k_l is the surface polarizability factor, which is a complex function of frequency, described for the lth grain by the following formula:

$$k_l = \frac{a_l}{2}(2\rho_l + \rho_0)(i\omega\tau_l)^{-C_l} \tag{3.7}$$

where τ_l is the time parameter; C_l is the relaxation parameter; and $\rho_l = \frac{1}{\sigma_l}$.

Substituting expressions 3.5, 3.6 and 3.7 into general formula 3.3, after some algebra, we arrive at the following GEMTIP model of the effective resistivity, ρ_e, for the multiphase composite medium with spherical grains:

$$\rho_{ef} = \rho_0 \left(1 + \sum_{l=1}^{N} \left(f_l m_l \left(1 - \frac{1}{1 + (-i\omega\tau_l)^{\mathrm{C_l}}}\right)\right)\right)^{-1} \tag{3.8}$$

where:

$$m_l = 3\frac{\rho_0 - \rho_l}{2\rho_l + \rho_0}, \rho_e = 1/\rho_e \tag{3.9}$$

The GEMTIP model has been successfully applied to mineral rocks (e.g., Zhdanov, 2008; Phillips, 2009) and hydrocarbon-bearing rocks (Buist, 2009a; Buist et al., 2009b; Burtman et al., 2009a, 2009b, 2010). The observed IP effects are within the 1 to 10^3 Hz band, leading us to conclude that relaxation processes in the milliseconds to seconds range should be typical for IP decay in mineral rocks, and faster for hydrocarbon-bearing samples.

In order to obtain the time-domain resistivity, one should apply the inverse Fourier transform to expression 3.8:

$$\rho_{ef}(t) = \frac{1}{2\pi}\int_{-\infty}^{\infty} \rho_{ef}(\omega) e^{i\omega t}\, \mathrm{d}\omega \tag{3.10}$$

CHAPTER 4

PRINCIPLES OF FORWARD MODELING AND INVERSION RESISTIVITY RELAXATION CURVE IN THE TIME DOMAIN

4.1 Forward Modeling: Cole-Cole Model

It was demonstrated in the pioneer work of Pelton (1977) that the Cole-Cole relaxation model (Cole and Cole, 1941) can represent well the typical complex conductivity of polarized rock formations. Buist (2009) demonstrated forward modeling of the Cole-Cole model with three IP parameters in the frequency domain. Phillips (2010) demonstrated that the new GEMTIP model can describe the IP effect as effectively as the time tested Cole-Cole model. This chapter shows in the time domain how varying IP parameters in each model changes the IP response in the data.

The Cole-Cole model is based on the assumption of bulk mineral discrimination and contains no information about rock composition. In the GEMTIP model, we take into account both physical and electrical characteristics of rocks at the grain scale using one analytic expression. These characteristics include grain size, grain shape, mineral conductivity, porosity, anisotropy, polarizability, mineral volume fraction, pore fluids, and more (Zhdanov, 2008).

In fact, the Cole-Cole appears as a special case of the GEMTIP model for a two-phase medium with spherical inclusions (Zhdanov, 2008).

To understand in more details what effect the three different IP parameters of the Cole-Cole model in the time domain have on synthetic data, different values of the three parameters shown in Tables 4.1, Table 4.2, and Table 4.3 have been modeled. Within these tables, two parameters are kept constant while the third parameter is varied. All parameters published data for a variety of common minerals (Buist, 2009).

Table 4.1. Cole-Cole parameters used for synthetic modeling when varying m.

Model	$\rho_0(DC)$	m	τ	C
No IP	500	*NA*	*NA*	*NA*
1	500	0.1	1	0.4
2	500	0.2	1	0.4
3	500	0.3	1	0.4
4	500	0.4	1	0.4
5	500	0.5	1	0.4
6	500	0.6	1	0.4

Table 4.2. Cole-Cole parameters used for synthetic modeling when varying τ.

Model	$\rho_0(DC)$	m	τ	C
No IP	500	*NA*	*NA*	*NA*
1	500	0.4	0.001	0.4
2	500	0.4	0.01	0.4
3	500	0.4	0.0	0.4
4	500	0.4	1	0.4
5	500	0.4	10	0.4
6	500	0.4	100	0.4

Table 4.3. Cole-Cole parameters used for synthetic modeling when varying C.

Model	$\rho_0(DC)$	m	τ	C
No IP	500	*NA*	*NA*	*NA*
1	500	0.4	1	0.1
2	500	0.4	1	0.2
3	500	0.4	1	0.3
4	500	0.4	1	0.4
5	500	0.4	1	0.5
6	500	0.4	1	0.6

Figure 4.1 depicts the case where the chargeability factor (m) is varied (from 0.1 for model 1, to 0.6 for model 6) it increases the slope of the resistivity. For a larger value of chargeability factor (m), the value of the resistivity is smaller. As time increases, the differences become close to the real resistivity. Changing m does not change the location (at what time) of the IP response, but only its amplitude. The slopes of the resistivity derivative with different chargeability factor (m) are quite similar.

In Figure 4.2, it shows that adjusting the time constant τ (from 0.001 seconds to 100 seconds) shifts the low value of resistivity response to a later time. Emond (2007) demonstrated that decreasing the grain size was analogous to decreasing the time parameter, which caused the IP effect to be at a lower frequency (later time). The behavior of the resistivity derivative is very interesting: in the early time ($t : 10^{-5} - 10^{4}$ seconds), increasing the time constant τ decreases the resistivity

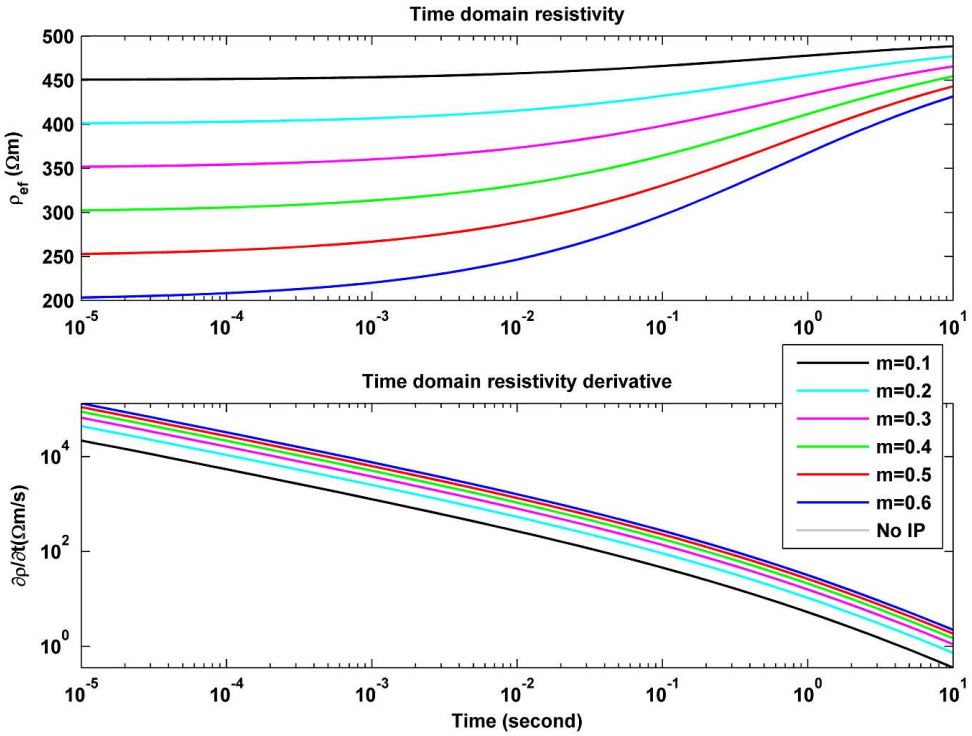

Figure 4.1. Resistivity and resistivity derivative behavior of the Cole-Cole model when the chargeability (m) factor varies from 0.1 to 0.6. Both the time constant (τ), and relaxation parameter (C) are held constant (1 second and 0.4, respectively).

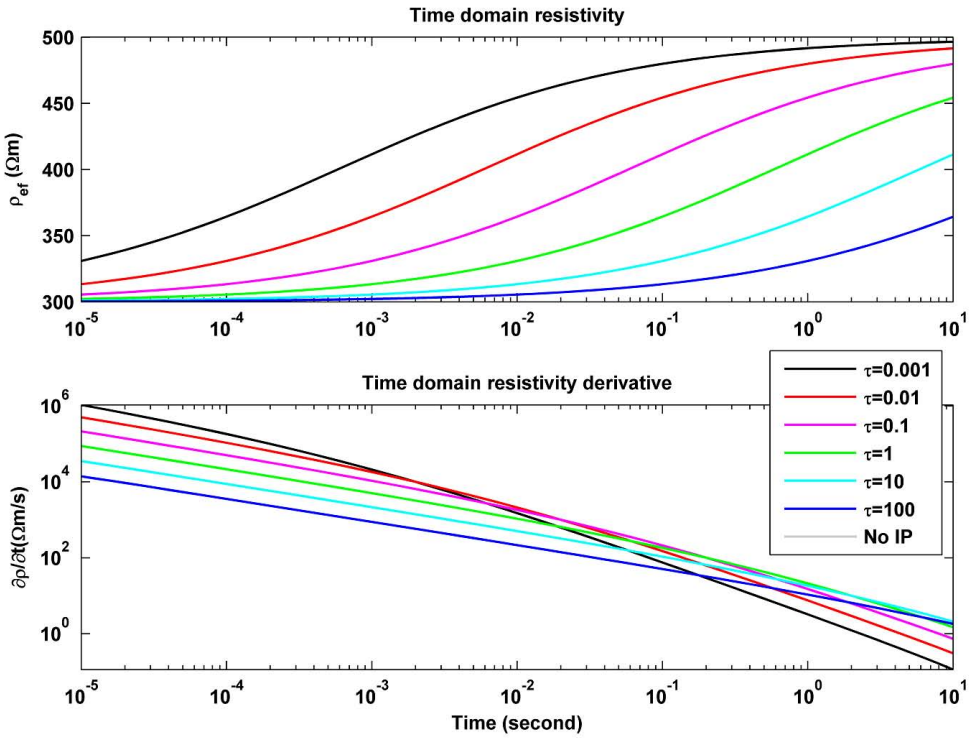

Figure 4.2. Resistivity and resistivity derivative behavior of the Cole-Cole model when the time constant (τ) varies from 0.001 to 100 seconds. Both the chargeability (m), and relaxation parameter (C) are held constant (0.4 and 0.4, respectively).

derivative; in the late time ($t : 1-10$ seconds), the larger time constant τ responses to the larger resistivity derivative value.

Figure 4.3 shows the effect that changing the relaxation parameter C, (from 0.1 to 0.6) has on the resistivity and resistivity derivative in the time domain. All plots of different relaxation parameter (C) converge at the time $t = 1$ second. The IP effect is more apparent for a larger relaxation parameter (C). For the resistivity derivative, in early time ($t10^5$ seconds), the smaller relaxation parameter (C) responses to a larger value of the resistivity derivative; in late time ($t : 1 - 10$ seconds), the larger relaxation parameter (C) responds to a larger value of the resistivity derivative.

From these results it is concluded that all of the three parameters affect the resistivity signature. However, the chargeability factor (m), which is the most important parameter in real life IP surveys, has a greater effect on the data over a long time range.

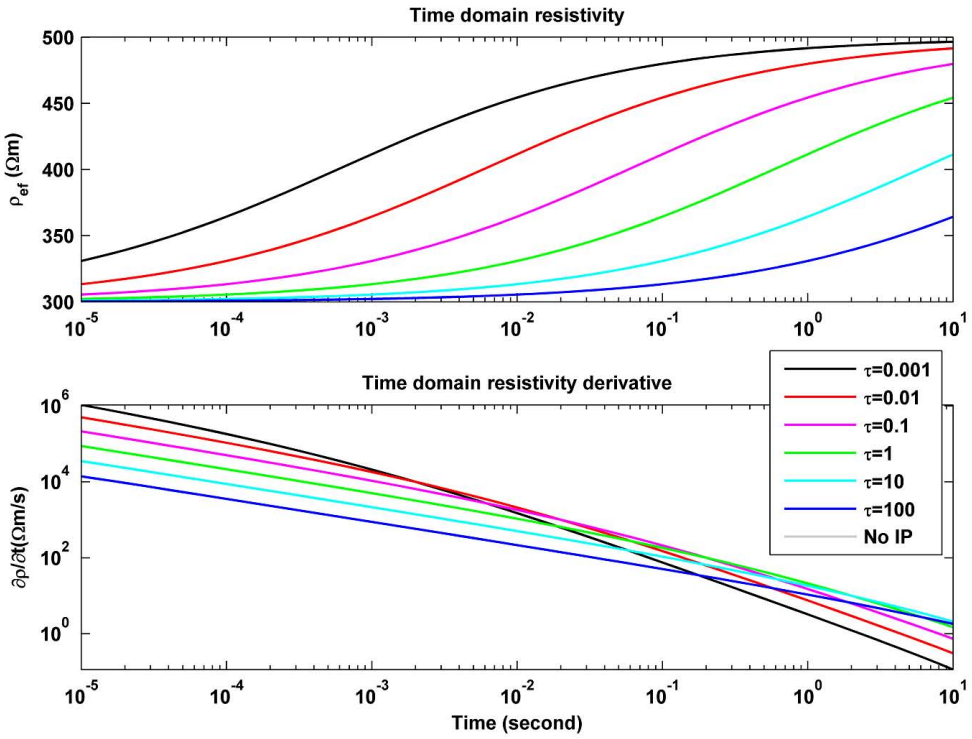

Figure 4.3. Resistivity and resistivity derivative behavior of the Cole-Cole model when the relaxation parameter (C) factor varies from 0.1 to 0.6. Both the time constant (τ), and chargeability parameter (m) are held constant (1 second and 0.4, respectively).

4.2 Forward Modeling: GEMTIP Model

In a special case of a simple two-phase heterogeneous model, formula (3.8) for the effective resistivity is simplified as (Zhdanov, 2008):

$$\rho_{ef} = \rho_0 \left(1 + \left(f_1 m_1 \left(1 - \frac{1}{1 + (-i\omega\tau_1)^{C_1}}\right)\right)\right)^{-1} \tag{4.1}$$

$$m_1 = 3\frac{\rho_0 - \rho_1}{2\rho_1 + \rho_0}, and \tau_1 = [\frac{a_1}{2\alpha_1}(2\rho_1 + \rho_0)]^{\frac{1}{C_1}} \tag{4.2}$$

In order to obtain the time domain resistivity, one should apply the inverse Fourier transform to expression 4.1:

$$\rho_{ef}(t) = \frac{1}{2\pi}\int_{-\infty}^{\infty} \rho_{ef}(\omega) e^{i\omega t}\, \mathrm{d}\omega \tag{4.3}$$

Figure 4.4 depicts the plot of the GEMTIP resistivity model, keeping all pa-

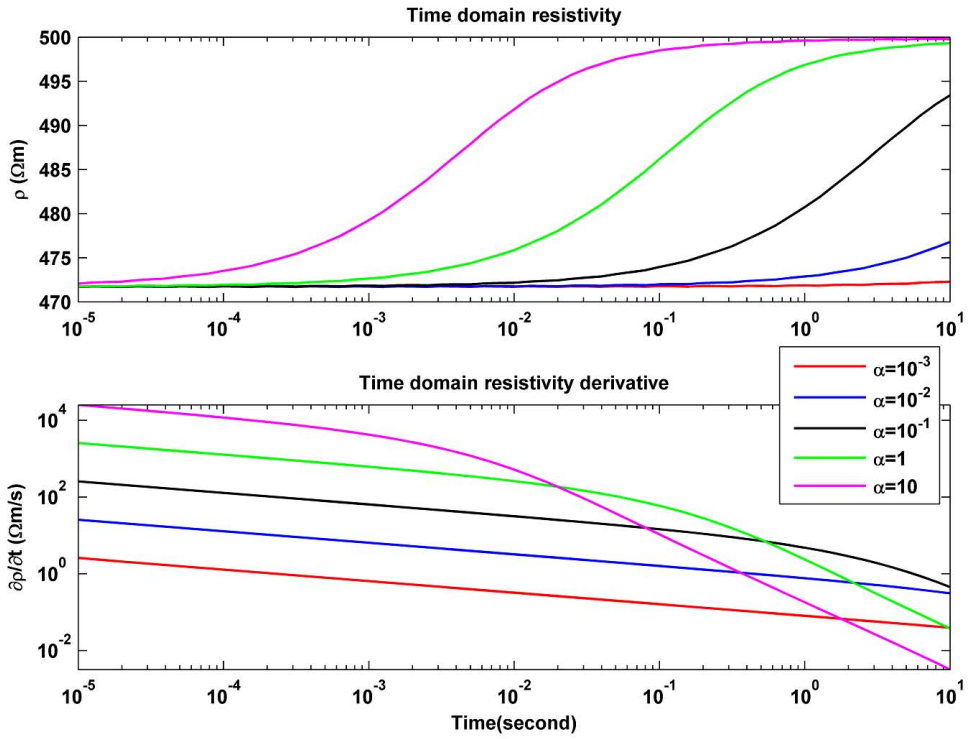

Figure 4.4. Spherical GEMTIP resistivity and resistivity derivative response obtained by maintaining all parameters constant but the surface polarizability coefficient (α).

rameters constant but the surface polarization coefficient. In this example, five different values of α are chosen to represent the range of reasonable values. It is very clearly shown that by varying α, the response of the computed resistivity shifts in time. High values of α correspond to early time response, while low values of α correspond to late time response. Also, varying α only affects the time at which IP effect appears.

Figure 4.5 shows how varying the decay coefficient (C) affects the computed resistivity values (while holding all other parameters constant). The decay coefficient (C) appears to affect resistivity response amplitude. Typical values for C range from 0 to 1. For low values of C, the resistivity response tends to decay gradually, which has high value of resistivity derivative in early time and low value in late time. In contrast, high values of C tend to cause a dramatic decrease of resistivity and more gradual slope of resistivity derivative.

In Figure 4.6, all parameters are kept constant except the volume fraction (f). By increasing f over several magnitudes, it clearly shows that the amplitude of the

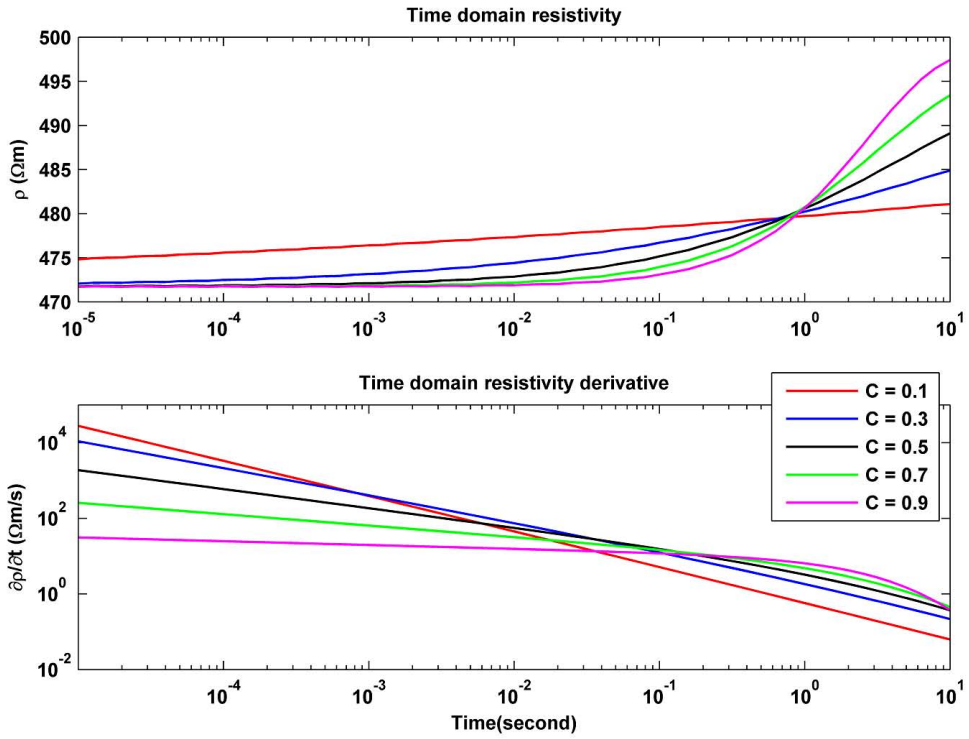

Figure 4.5. Spherical GEMTIP resistivity and resistivity derivative response obtained by maintaining all parameters constant but the surface delay coefficient (C)

resistivity response significantly increases proportionately. High values of volume fraction (f) have high values of resistivity derivative. Understanding the effects of the volume fraction is particularly significant because it is one the parameters that can be measured directly.

4.3 Analytical Solutions for the Time Domain GEMTIP Model

We now consider a few cases where the Fourier transformation (4.3) results in the analytical expression for the effective resistivity.

For example, in the case of $C_1 = 1$, equation 4.1 can be rewritten as:

$$\rho_{ef}(\omega) = \frac{\rho_0}{1 + (1 + f_1 m_1) i\omega\tau_1} + \frac{\rho_0 i\omega\tau_1}{1 + (1 + f_1 m_1) i\omega\tau_1} \tag{4.4}$$

By introducing a new constant,

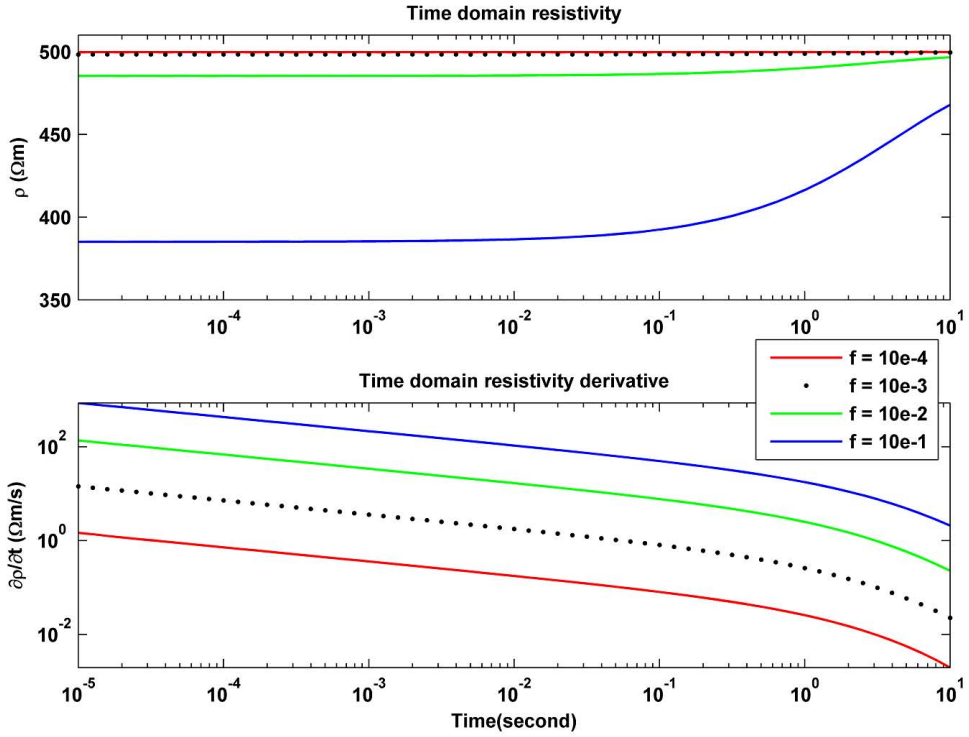

Figure 4.6. Spherical GEMTIP resistivity and resistivity derivative response obtained by maintaining all parameters constant but the volume fraction (f).

$$k = 1 + f_1 m_1 \tag{4.5}$$

We can also write:

$$\rho_{ef}(\omega) = \frac{\rho_0}{1 + ki\omega\tau_1} + \frac{\rho_0 i\omega\tau_1}{1 + ki\omega\tau_1} \tag{4.6}$$

According to Abramowitz and Stegun (1964), the first term in equation 4.6 has the Fourier transform pair for $\alpha > 0$:

$$\frac{1}{\alpha + i\omega} \rightarrow u(t)e^{-t} \tag{4.7}$$

where $u(t)$ is the Heaviside unit step function, $u(t) = 1$, $t > 0$. For conversion of the second term in equation 4.6, we use a time differentiation property of the Fourier transform:

$$i\omega F(\omega) \rightarrow \frac{d[f(t)]}{dt} \tag{4.8}$$

For the inverse Fourier transform, we use a scaling property of the Fourier transform:

$$\frac{1}{|a|}\left(\frac{\omega}{a}\right) \rightarrow f(at) \tag{4.9}$$

where a is a constant. We can now write:

$$\frac{k\tau_1}{k\tau_1}\frac{\rho_0}{1+ki\omega\tau_1} \rightarrow \frac{\rho_0}{k\tau_1}\exp\left(-\frac{t}{k\tau_1}\right) \tag{4.10}$$

Since

$$\frac{d}{dt}\left[\frac{\rho_0}{k\tau_1}\exp\left(-\frac{t}{k\tau_1}\right)\right] = \frac{\rho_0}{(k\tau_1)^2}\exp\left(-\frac{t}{k\tau_1}\right) \tag{4.11}$$

The second term in equation 4.6 could be transformed by using equation 4.8:

$$\frac{k\tau_1}{k\tau_1}\frac{\rho_0 i\omega\tau_1}{1+ki\omega\tau_1} \rightarrow \frac{\rho_0\tau_1}{(k\tau_1)^2}\exp\left(-\frac{t}{k\tau_1}\right) = \frac{\rho_0}{k^2\tau_1}\exp\left(-\frac{t}{k\tau_1}\right) \tag{4.12}$$

Exploiting linearity of the Fourier transform, and using equations 4.11 and 4.12, we arrive at the analytical expression for GEMTIP in the time domain for $C_1 = 1$ as:

$$\rho_{ef}(t) = \frac{\rho_0}{k\tau_1}\exp\left(-\frac{t}{k\tau_1}\right) + \frac{\rho_0}{k^2\tau_1}\exp\left(-\frac{t}{k\tau_1}\right) \tag{4.13}$$

Or substituting back, $k = 1 + f_1 m_1$:

$$\rho_{ef}(t) = \frac{\rho_0}{(1+f_1 m_1)\tau_1} \exp\left(-\frac{t}{(1+f_1 m_1)\tau_1}\right) + \frac{\rho_0}{(1+f_1 m_1)^2 \tau_1} \exp\left(-\frac{t}{(1+f_1 m_1)\tau_1}\right) \quad (4.14)$$

Figure 4.7 compares the analytic solution of the time-domain GEMTIP response with a discrete Fourier transform of the frequency-domain GEMTIP responses for the same material parameters. Diversion of the analytic and discrete solutions can be explained by boundary conditions used in the Fourier transform, and accuracy of the digital filters.

As a second analytical example we consider the case where $C_1 = 2$. Following similar algebra, as used for equations 4.1 through 4.14, it can be shown that the analytic solution for this case is given by:

$$\rho_{ef}(t) = \frac{\rho_0}{(1+f_1 m_1)\tau_1} \sin\left(-\frac{t}{(1+f_1 m_1)\tau_1}\right) + \frac{\rho_0}{(1+f_1 m_1)^2 \tau_1} \sin\left(-\frac{t}{(1+f_1 m_1)\tau_1}\right) \quad (4.15)$$

It can also be shown that an approximate time-domain GEMTIP solution for $C_1 = 0.5$ could be written as follows:

$$\rho_{ef}(t) = \frac{\rho_0}{(1+f_1 m_1)\tau_1} erfc\left(\sqrt{-\frac{t}{(1+f_1 m_1)\tau_1}}\right) \exp\left(-\frac{t}{(1+f_1 m_1)\tau_1}\right) + \frac{\rho_0}{(1+f_1 m_1)^2 \tau_1} erfc\left(\sqrt{-\frac{t}{(1+f_1 m_1)\tau_1}}\right) \exp\left(-\frac{t}{(1+f_1 m_1)\tau_1}\right) \quad (4.16)$$

where $erfc$ is the complementary error function defined by the following formula:

$$erfc = 1 - erf(x) = 1 - \frac{2}{\sqrt{x}} \int_0^x \exp(-y^2) \mathrm{d}y \quad (4.17)$$

4.4 Regularized Conjugate Gradient Method

It is known that modeling the IP effect is very useful in improving mineral discrimination techniques. With improved understanding of the IP effect and

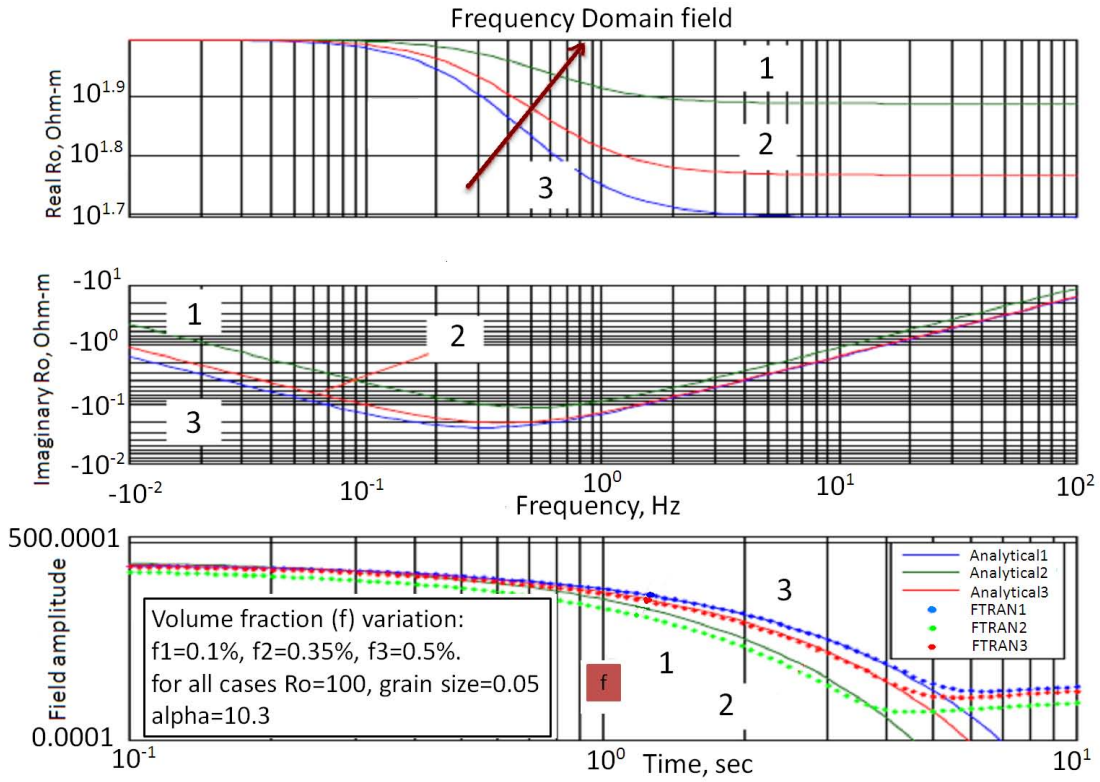

Figure 4.7. Comparison between the analytic solutions of the GEMTIP resistivity relaxation models in the time domain and the results of the numerical Fourier transform (FTRAN) of the corresponding GEMTIP resistivity curves in the frequency domain. A comparison is shown for three models with different volume fraction of the polarizable grains: $f_1 = 0.1\%$, $f_2 = 0.35\%$, and $f_3 = 0.5\%$. The top and middle panels show the real and imaginary parts of the resistivity relaxation curves in the frequency domain. The corresponding time-domain solutions are shown in the bottom panel. The solid lines correspond to the analytic solution, while the dotted lines correspond to the numerical Fourier transform of the frequency-domain GEMTIP model. The following parameters were used: $\rho_0 = 1000Ohm - m$, $a_1 = 0.005m$, and $\rho_1 0 = 1Ohm - m$. The brown arrow in the upper and bottom panels show the increase of the volume fraction.

new advancements in rock physics models, mineral discrimination will become more effective as well as more reliable. As shown in forward modeling, different parameters of the GEMTIP model control different behaviors of the IP effect. So obtaining the recovered values of parameters from inversion can be quite useful.

An inverse problem can be formulated as the solution of the operator equation:

$$\mathbf{d} = A(\mathbf{m}) \tag{4.18}$$

where $\mathbf{m}$ is some function (or vector) describing the model parameters, $\mathbf{d}$ is the data set and A is the operator of forward modeling.

The problems in this research are ill-posed and unstable. To find the stable solution for the minimization problem, we have to consider the regularized minimization of the Tikhonov parametric functional:

$$P^{\alpha}(\mathbf{m}) = \rho_D^2(A(\mathbf{m}), \mathbf{d}) + \alpha s(\mathbf{m}) = min \tag{4.19}$$

where $s(\mathbf{m})$ is some stabilizing functional.

The iteration process of the regularized conjugate gradient (RCG) method is based on the calculation of the regularized steepest descent directions:

$$\mathbf{m}_{n+1} = \mathbf{m}_n + \delta\mathbf{m}_n - \tilde{k}_n^{\alpha}\tilde{\mathbf{l}}^{\alpha}(\mathbf{m}_n). \tag{4.20}$$

First, the direction of regularized steepest ascent is used:

$$\tilde{\mathbf{l}}^{\alpha}(\mathbf{m}_0) = \mathbf{l}^{\alpha}(\mathbf{m}_0). \tag{4.21}$$

The next direction is a linear combination of the regularized steepest ascent in this step, and the conjugate gradient direction in the previous step:

$$\tilde{\mathbf{l}}^{\alpha}(\mathbf{m}_1) = \mathbf{l}^{\alpha}(\mathbf{m}_1) + \beta_1^{\alpha}\tilde{\mathbf{l}}^{\alpha}(\mathbf{m}_0). \tag{4.22}$$

The steps $\tilde{k}_n^{\alpha}$ are selected based on the minimization of the parametric functional:

$$P^{\alpha}(\mathbf{m}_{n+1}) = P^{\alpha}(\mathbf{m}_n) - \tilde{k}_n^{\alpha}\mathbf{l}^{\alpha}(\mathbf{m}_n) = \Phi(\tilde{k}_n^{\alpha}). \tag{4.23}$$

Minimization of this functional gives the following best estimation for the length of the step using a linear line search:

$$\begin{aligned}\tilde{k}_n^\alpha &= (\tilde{\mathbf{l}}_n^\alpha, \mathbf{l}_n^\alpha)/(\tilde{\mathbf{l}}_n^\alpha, F_{mn}^* F_{mn} + \alpha(W^*W)\tilde{\mathbf{l}}_n^\alpha) \\ &= (\tilde{\mathbf{l}}_n^\alpha, \mathbf{l}_n^\alpha)/[(F_{mn}\tilde{\mathbf{l}}_n^\alpha, F_{mn}\tilde{\mathbf{l}}_n^\alpha) + \alpha(W\tilde{\mathbf{l}}_n^\alpha, W\tilde{\mathbf{l}}_n^\alpha)] \\ &= (\tilde{\mathbf{l}}_n^\alpha, \mathbf{l}_n^\alpha)/[||F_{mn}\tilde{\mathbf{l}}_n^\alpha||^2 + \alpha||W\tilde{\mathbf{l}}_n^\alpha||^2] \end{aligned} \tag{4.24}$$

The β_n coefficients are determined by the following formula:

$$\beta_n^\alpha = ||\mathbf{l}^\alpha(\mathbf{m}_n)||^2/||\mathbf{l}^\alpha(\mathbf{m}_{n-1})||^2. \tag{4.25}$$

The final numerical scheme for the RCG method can be summarized as follows:

$$\begin{aligned} \mathbf{r}_n &= A(\mathbf{m}_n) - d, \\ \mathbf{l}_n^\alpha = \tilde{\mathbf{l}}^\alpha(\mathbf{m}_n) &= F_{mn}^* \mathbf{r}_n + \alpha W^* W(\mathbf{m}_n - \mathbf{m}_{apr}), \\ \beta_n^\alpha &= ||\mathbf{l}_n^\alpha||^2/||\mathbf{l}_{n-1}^\alpha||^2, \\ \tilde{\mathbf{l}}_n^\alpha &= \mathbf{l}_n^\alpha + \beta_n^\alpha \tilde{\mathbf{l}}_{n-1}^\alpha, \\ \tilde{\mathbf{l}}_0^\alpha &= \mathbf{l}_0, \\ \tilde{k}_n^\alpha &= (\tilde{\mathbf{l}}_n^\alpha, \mathbf{l}_n^\alpha)/[||F_{mn}\tilde{\mathbf{l}}_n^\alpha||^2 + \alpha||W\tilde{\mathbf{l}}_n^\alpha||^2], \\ \mathbf{m}_{n+1} &= \mathbf{m}_n - \tilde{k}_n^\alpha \tilde{\mathbf{l}}_n^\alpha. \end{aligned} \tag{4.26}$$

The initial regularization parameter α is calculated using the following formula:

$$\alpha = \frac{||A(\mathbf{m}_1) - \mathbf{d}||^2}{||\mathbf{m}_1 - \mathbf{m}_{apr}||^2}. \tag{4.27}$$

We also implement the adaptive regularization; therefore, α_n becomes

$$\alpha_n = \alpha q^n, \tag{4.28}$$

where:

$$0 < q < 1. \tag{4.29}$$

The numerical scheme has been implemented using a MATLAB code.

4.5 Inversion: GEMTIP Model

4.5.1 Model 1: Two-phase GEMTIP model

The synthetic data are obtained from the forward modeling considering one disseminated phase that occurs at one grain size. The matrix resistivity of the rock is 100 m. The resistivity of the inclusions is 0.1 Ωm, which represents pyrite. All the inclusions are spherical with the same radius ($a = 2\ mm$). The volume fraction of the inclusions is 5.0%. The values of the decay and surface polarizability coefficients are 0.5 and 0.4 $(\Omega m^2)/sec^c$, respectively. All the parameters are summarized in Table 4.4.

Figure 4.8 shows the effective resistivity plotted against time. The solid dots and hollow boxes represent original and predicted data. The original observed data come from using the true model parameter values, while the predicted data are determined by minimizing the Tikhonov parametric functional using the RCG method with initial conditions. It clearly shows that the predicted data fit the original observed data very well.

Figure 4.9 shows the converging model steps plotted over the misfit functional. In the regularized inversion, a relaxation coefficient of $q = 0.9$ is used. The misfit threshold is set to 0.1%. And after 100 iterations, the misfit reaches 0.1%. After inversion, the correct surface polarizability (α) is recovered from 1 to 0.40, while the decay coefficient (C) is recovered from 1 to 0.50.

4.5.2 Model 2: Two-phase GEMTIP model with 2% random noise

We have now added 2% random noise to the data while all the parameters are kept the same as in the previous synthetic model. The original and predicted resistivity in time and the misfit against iteration number are illustrated in Figure 4.10 and Figure 4.11. After 100 iterations, the misfit becomes 0.3%. And the

Table 4.4. GEMTIP inversion parameters.

Variable	Units	True model	Initial	Recovered
ρ_{matrix}	Ωm	400	-	-
f	-	0.08	-	-
C	Seconds	0.5	1.0	0.50
ρ_{phase1}	$\Omega\ m$	0.3	-	-
a	mm	12.5	-	-
α	$\frac{\Omega \cdot m^2}{sec^{cl}}$	0.4	1.0	0.40

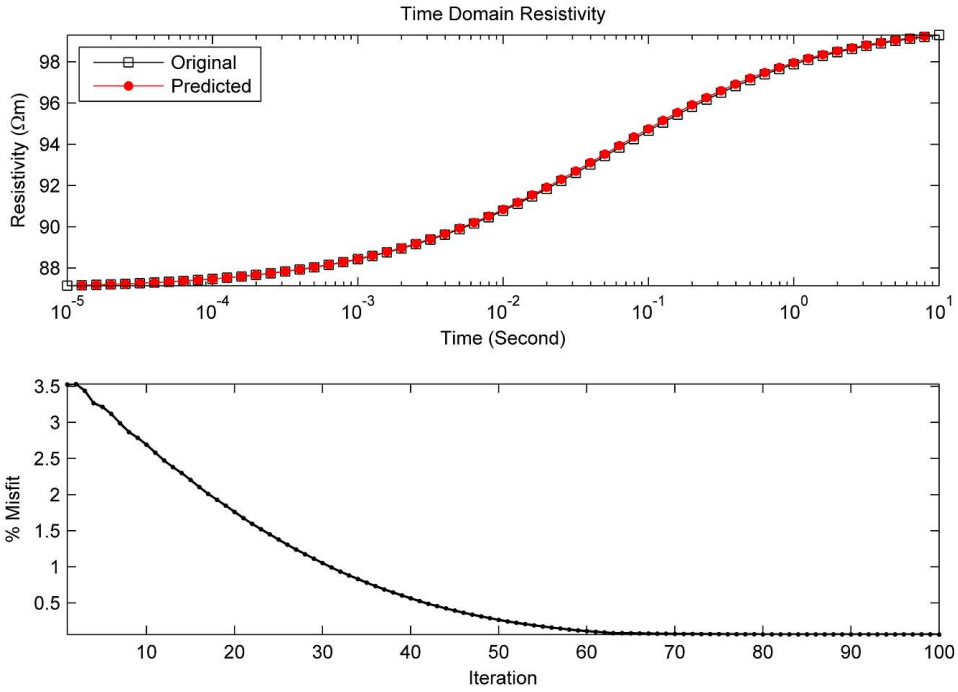

Figure 4.8. Synthetic model. a) The effective resistivity plotted against time from $10^{-5}s$ - $10s$. b) Percent misfit against number of iterations from inversion.

surface polarizability (α) is recovered from 1 to 0.41, while the decay coefficient (C) is recovered from 1 to 0.52.

4.5.3 Model 3: Three-phase GEMTIP model

Figure 4.12 represents both the original and predicted resistivity curves in the time domain for the three-phase GEMTIP model. The synthetic data are obtained from the forward modeling considering a model formed by a homogeneous host rock filled with two types of spherical grains, simulating, e.g., pyrite and chalcopyrite inclusions. The matrix resistivity of the rock is 300 Ωm.

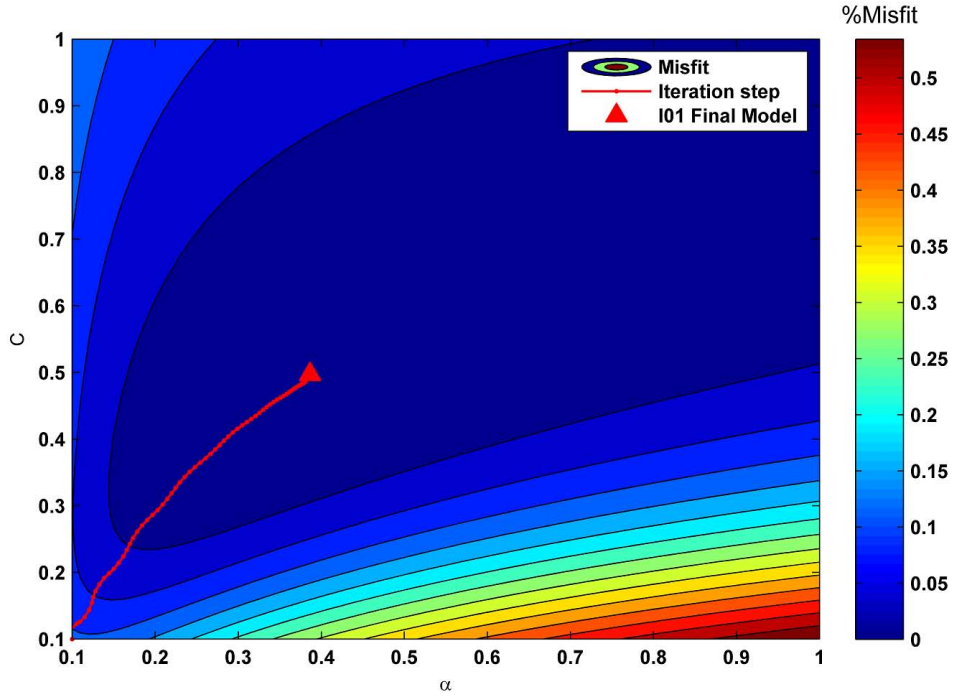

Figure 4.9. Synthetic model. The misfit functional is plotted with shaded isolines signifying the direction of decreasing misfit. Model steps are also plotted and are shown to converge after several iterations.

The resistivity of these two grains are $\rho_1 = 0.2\Omega m$ and $\rho_1 = 0.004\Omega m$, respectively. And the inclusions have different radii ($a_1 = 0.2mm$ and $a_2 = 0.8mm$). The volume fraction of the inclusions are both 15.0%. The values of the decay and surface polarizability coefficients are 0.8, 0.6 and $2\frac{\Omega \cdot m^2}{sec^{c_l}}$, $0.04\frac{\Omega \cdot m^2}{sec^{c_l}}$ respectively. All the parameters are summarized in Table 4.5. The recovered delay and surface polarizability are almost the same as true value.

The original observed data come from using the true model parameter values, while the predicted data are determined by minimizing the Tikhonov parametric functional using the RCG method with initial conditions. We notice that in the case of multiphase model, the resistivity curve in the time domain becomes more complicated than the conventional Cole-Cole curve. After 91 iterations, the misfit becomes less than 0.02%. It clearly shows that the predicted data fit the original observed data very well.

In order to compare the inversion results in the time domain and in the frequency domain, I will present the original and predicted resistivity curves in the frequency

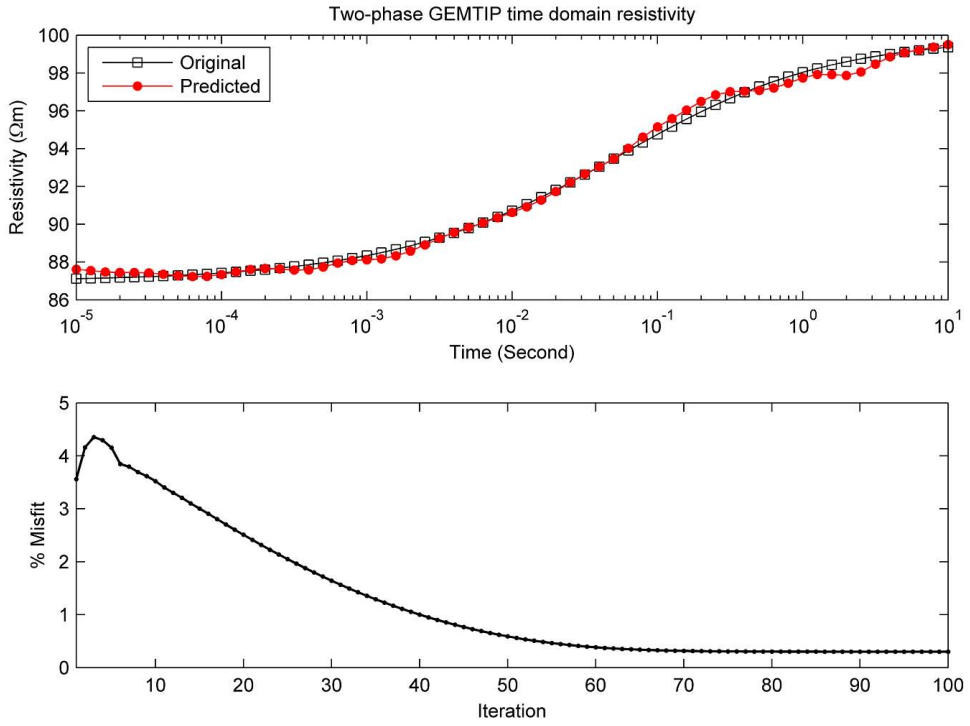

Figure 4.10. Synthetic sample with 2% random noise. a). The effective resistivity plotted against time from $10^{-5}s - 10s$. b). Percent misfit against number of iterations from inversion.

domain for the three-phase GEMTIP model. All the parameters are the same as those in the time domain.

Figure 4.13 shows the inversion result in the frequency domain. At the frequency 10^{-2} Hz, 1 Hz and 11 Hz, the predicted resistivities do not fit the original resistivities well. And in Table 4.6, the inversion result is not as good as that in the frequency domain: the recovered parameters are a little different from the true values. The surface polarizability of the first type inclusions (α_1) is not well recovered after inversion. The effect of the first type inclusion is shown as the peak in the imaginary part of the resistivity at the frequency 10^{-2} Hz. Obviously, the original imaginary part of the resistivity is about 4 Ωm higher than the predicted value at the frequency 10^{-2} Hz, which can explain why the inversion result of α_1 is not good. Similarly, the difference between the original and predicted imaginary part of the resistivity at the frequency 11 Hz reflects the difference between the recovered and true value of the surface polarization α_2.

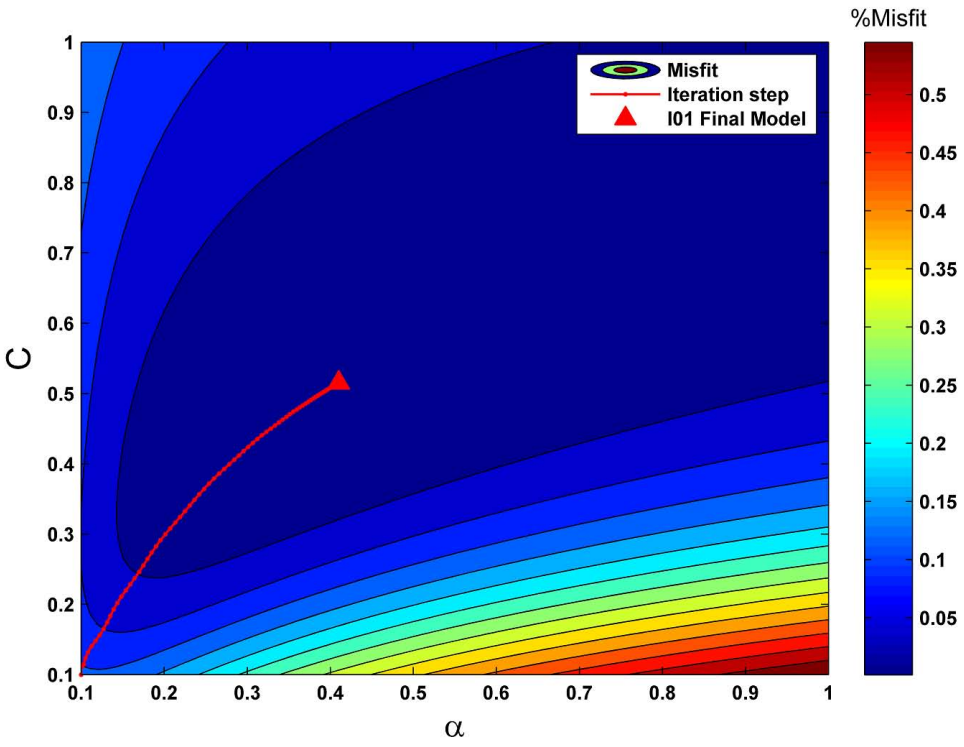

Figure 4.11. Synthetic sample with 2% random noise. The misfit functional is plotted with shaded isolines signifying the direction of decreasing misfit. Model steps are also plotted and are shown to converge after several iterations.

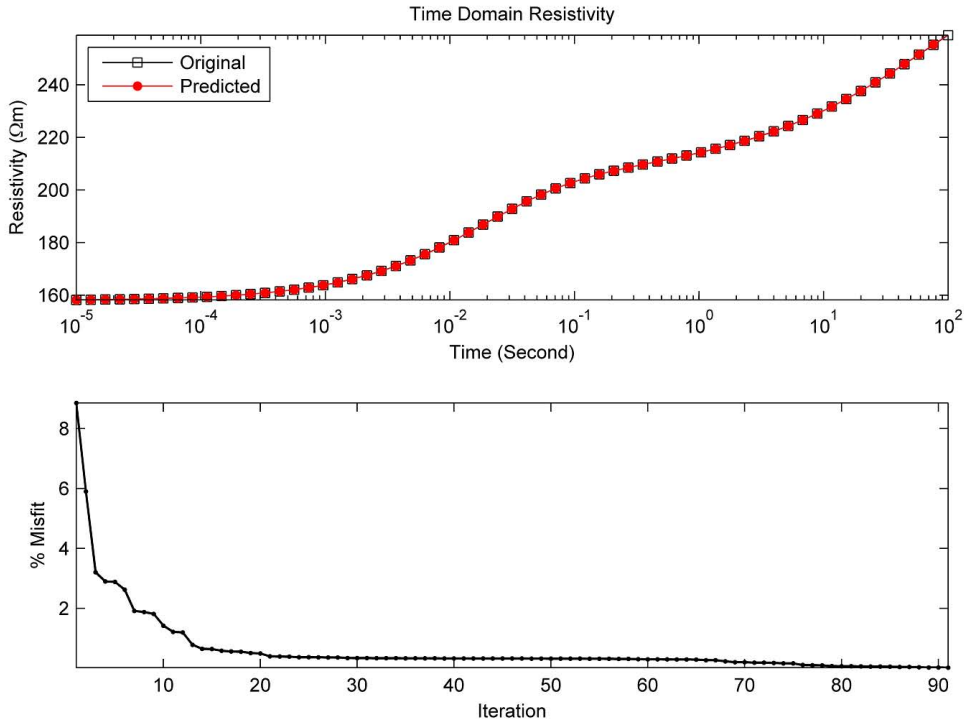

Figure 4.12. Synthetic three-phase GEMTIP model. The original and predicted resistivity plotted against time from $10^{-5}s - 10^{2}s$. The lower panel is percent misfit against number of iterations from the inversion.

Table 4.5. Three-phase GEMTIP model inversion parameters in the time domain

Variable	**Units**	**True model**	**Initial**	**Recovered**
ρ_0	Ωm	300	-	-
f_1	%	15	-	-
f_2	%	15	-	-
ρ_1	$\Omega\ m$	0.2	-	-
ρ_2	$\Omega\ m$	0.004	-	-
a_1	mm	0.2	-	-
a_2	mm	0.8	-	-
C_1	Seconds	0.8	1.0	0.80
C_2	Seconds	0.6	1.0	0.60
α_1	$\frac{\Omega \cdot m^2}{sec^{cl}}$	2	3	1.99
α_2	$\frac{\Omega \cdot m^2}{sec^{cl}}$	0.04	0.2	0.04

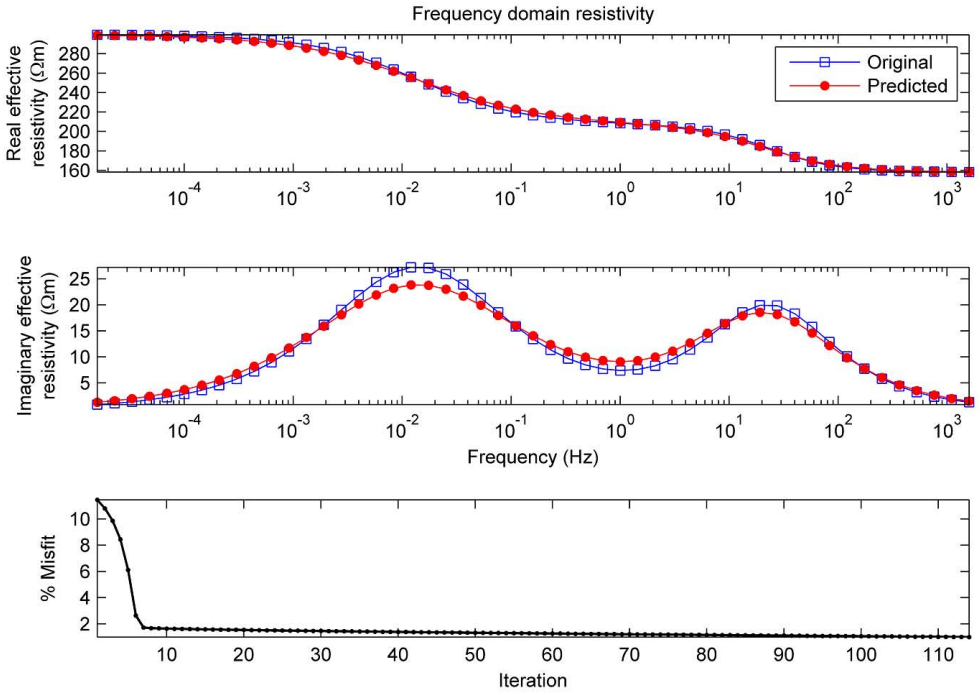

Figure 4.13. Synthetic three-phase GEMTIP model. The original and predicted resistivity plotted against time from 10^{-5} Hz - 10^{3} Hz. The lower panel is percent misfit against number of iterations from the inversion.

Table 4.6. Three-phase GEMTIP model inversion parameters in the frequency domain

Variable	**Units**	**True model**	**Initial**	**Recovered**
ρ_0	Ωm	300	-	-
f_1	%	15	-	-
f_2	%	15	-	-
ρ_1	$\Omega\ m$	0.2	-	-
ρ_2	$\Omega\ m$	0.004	-	-
a_1	mm	0.2	-	-
a_2	mm	0.8	-	-
C_1	Seconds	0.8	1.0	0.86
C_2	Seconds	0.6	1.0	0.67
α_1	$\frac{\Omega \cdot m^2}{sec^{cl}}$	2	3	2.88
α_2	$\frac{\Omega \cdot m^2}{sec^{cl}}$	0.04	0.2	0.03

CHAPTER 5

ANALYSIS OF EXPERIMENTAL DATA

This chapter analyzes the experimental data obtained from the electron microtomography equipment QEMSCAN imaging and X-ray micro tomography. The rock samples were measured at the University of Utah. The complex resistivity data were measured at Zonge Engineering and Research Organization, Inc. A description and analysis of these samples will be made in this chapter.

5.1 Description of the Samples

5.1.1 Sample K01

Sample K01 is dacite from the Kori Kollo mine in Bolivia with disseminated pyrite (FeS_2) in a predominantly sericite and quartz matrix (Figure 5.1). This igneous rock was selected because of the mineral inclusions that are potentially ideal for analysis by the GEMTIP rock physics model.

For better understanding of the 3-D structure and composition, sample K01 was analyzed using three-dimensional (3D) X-ray microtomography (Emond, 2007). The X-ray microtomography created a 3D volume of attenuation coefficients. The attenuation coefficients were used to distinguish the pyrite from the rock matrix. In addition to the 3D image, the volume fraction, inclusion size, and surface area can be determined by X-ray microtomography. A summary of the X-ray microtomography can be seen in Table 5.1. For example, a 3D microtomographic image of sample K01 is shown in Figure 5.2, and highlights the sulfide phases.

5.1.2 Sample #13

Sample #13 is a porphyry copper deposit from the mines at Sar Cheshmeh in Iran, which is the worlds second largest porphyry copper deposit (5% of the worlds total). The sample contains disseminated chalcocite (Cu_2S), chalcopyrite ($CuFeS_2$), and pyrite (FeS_2) in a predominantly feldspar, quartz, and mica matrix.

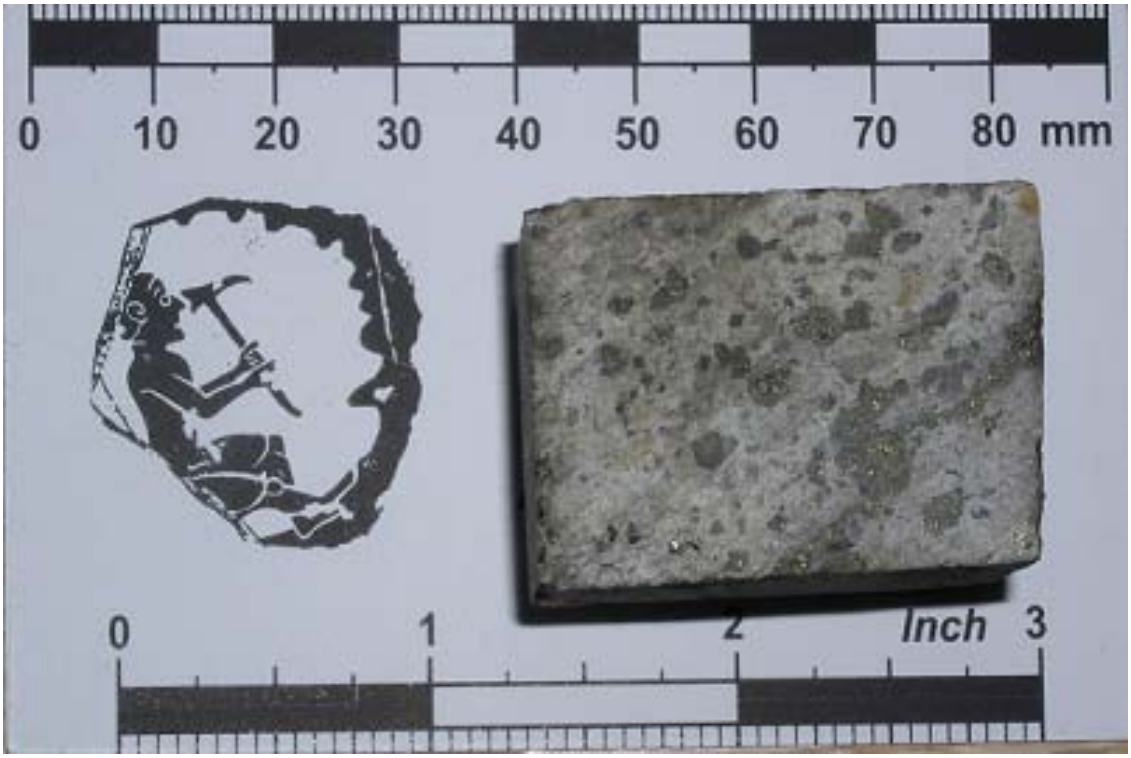

Figure 5.1. Sample K01 contains disseminated pyrite (size: about $2mm$). Monzonite from the Kori Kollo mine, Bolivia.

Table 5.1. K01 mineralogical summary (Emond, 2007)

Method	Matrix Composition	Pyrite Vol. fraction	Pyrite radius
Optical	sericite, quartz	10%	$1 - 2.5mm$
X-ray	quantitative	7%	478 inclusions. 90% volume from 0.5 to $1.3mm$
X-ray	quantitative	-	Predominantly 1 to $2mm$ with smaller grains

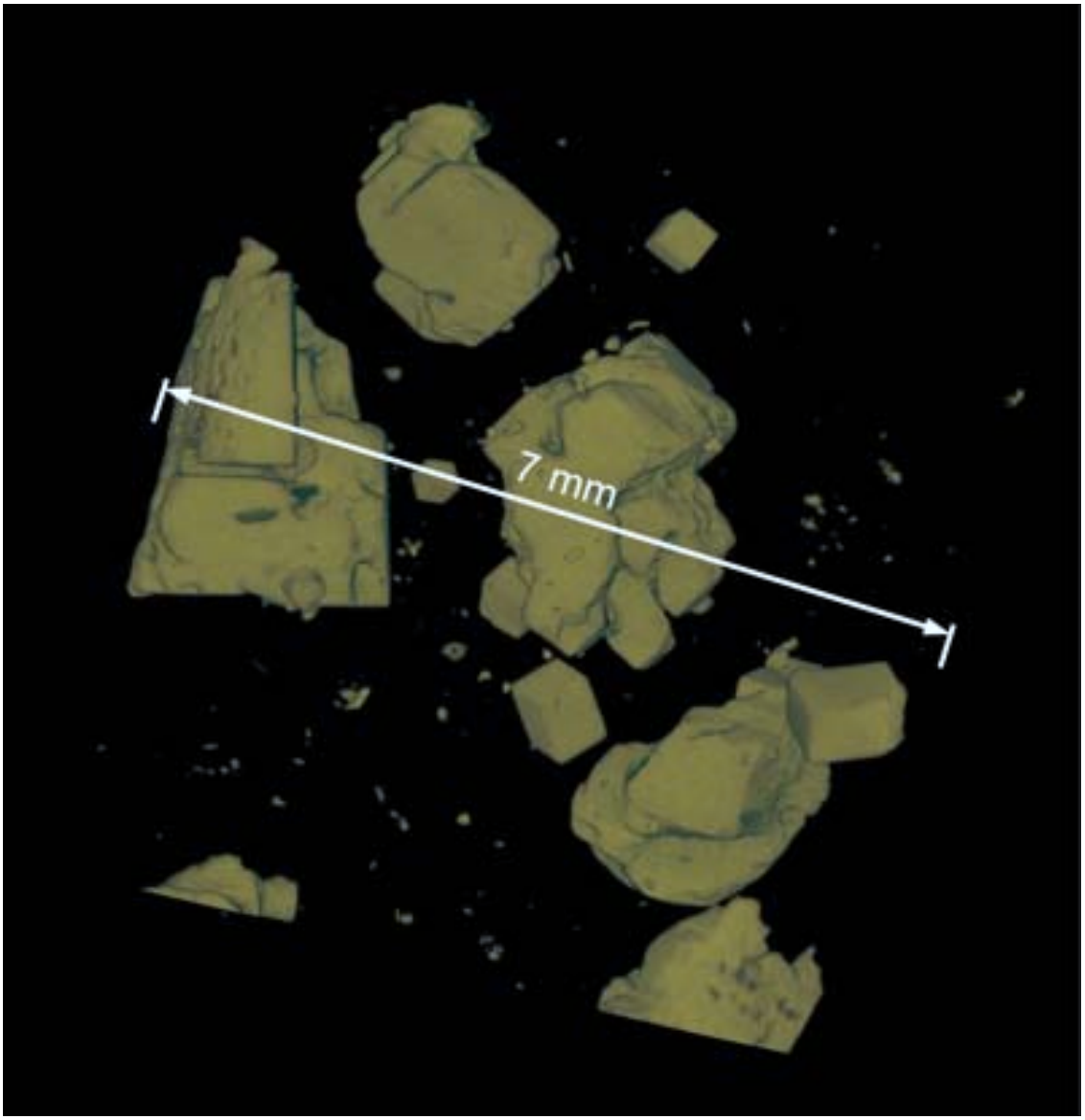

Figure 5.2. X-ray tomography image of Sample K01, Korri Kollo, Bolivia, pyrite in a sericite and quartz matrix. The image has been optimized to show the pyrite (Emond, 2007).

Sample #13 is shown in Figure 5.3 and Figure 5.4. The shiny spots are chalcopyrite and pyrite inclusions. All sulfides are introduced during micro vein formation (introduction of quartz). Later during supergene enrichment chalcopyrite is partially replaced by chalcocite. Pyrite is not attacked by chalcopyrite. K-feldspar phenocrysts are altered to muscovite. The rest of the rock consists of K-feldspar and quartz.

5.2 QEMSCAN Measurement

Five samples (#13, TC-7F, B5, WL5 and WL3) have been analyzed using the QEMSCAN at the University of Utah department of Geology and Geophysics. A detailed mineralogical analysis of samples can be obtained with QEMSCAN. Four Energy Dispersive Spectrometry (EDS) detectors are used simultaneously to decrease the time required to analyze samples. Polished samples are coated with a thin layer of carbon, scanned for mineral composition and size. A color coded image of mineral composition is created as well as a quantitative measurement of mineral abundance and inclusion size.

Figure 5.5 of Sample #13 is acquired by QEMSCAN measurement. It is a representative section of sample #13. The sample contains 3.09% chalcocite, 0.46% chalcopyrite, 0.02% pyrrhotite, 30.2% quartz and 64.4% feldspars and mica.

5.3 Complex Resistivity Measurements

Complex resistivity measurements were obtained from Zonge Engineering and Research Organization Inc, Tuscon, Arizona. The frequency domain data were collected over a range from about 0.03 Hz to about 2300 Hz. The time domain data were measured at frequencies of 0.125 Hz, 1 Hz and 32 Hz. Samples #13, WL3 and TC-7F were measured twice in two orthogonal directions. This was done to test whether the anisotropy of the bedding in these samples would have an actual effect on the measured resistivity. Analyzing these samples with the GDP16 required special preparation procedures. First, each sample had to be trimmed to approximately one inch square to fit appropriately between the current electrodes. Second, if the sample was measured dry, the resistivity data collected would be meaningless, because the electrodes and the rock sample are not well contacted. Thus, in order for the electrolytes to flow through the porous volume of the sample,

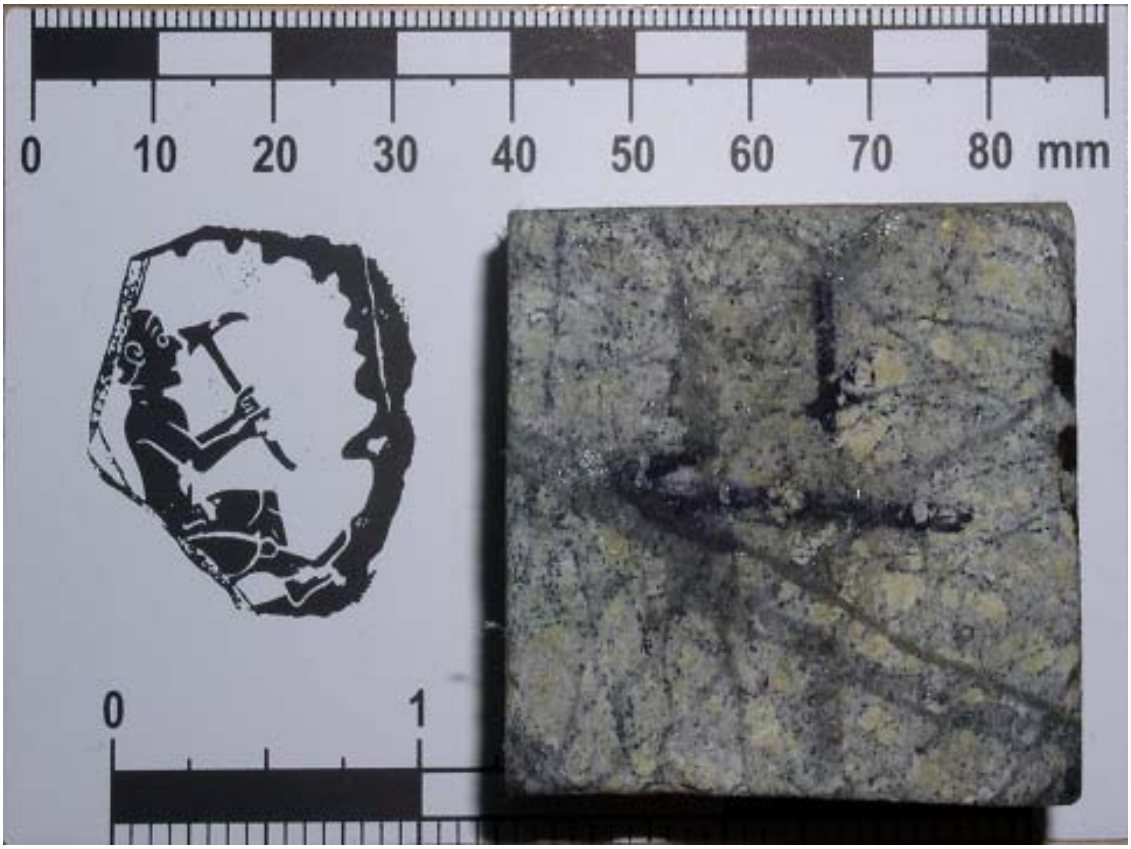

Figure 5.3. Porphyry copper deposit from Sarchesme, Iran with disseminated chalcocite (Cu_2S), chalcopyrite ($CuFeS_2$), and pyrite (FeS_2). The first measurement is in the labeled direction.

it had to be soaked in water for approximately three days before the measurement. Additionally, the electrodes and the rock samples should be contacted in copper sulfate solution for about 10 minutes before starting the measurement. These two procedures were followed for each sample that was measured. The equipment used to perform these measurements is shown in Figures 5.6 and 5.7.

The plots of the raw resistivity data in the frequency domain recorded at Zonge are shown in Figure 5.8 and 5.9 for samples K01 and #13, respectively. Two sets of data were recorded for these two samples. Unfortunately, one difficulty arises when using the GDP16 to record complex resistivity, which is that the resistivity measurements for a given sample tend to shift to lower values as more measurements are made. This may be explained by the increased penetration of the electrolytes via the copper sulfate solution flowing into the porous regions of the rock sample as time passes. At the same time, the measured resistivity values also may increase as time passes because of the porous membranes getting dry.

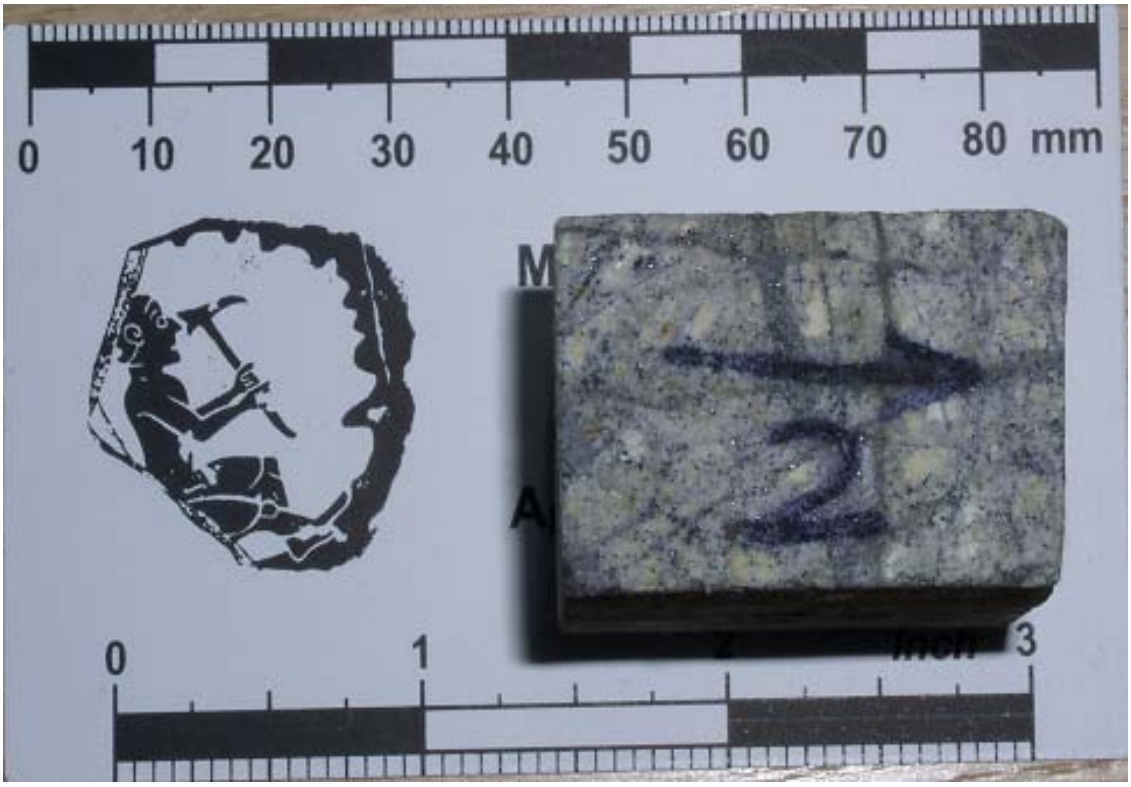

Figure 5.4. The second measurement of sample #13 is in the labeled direction.

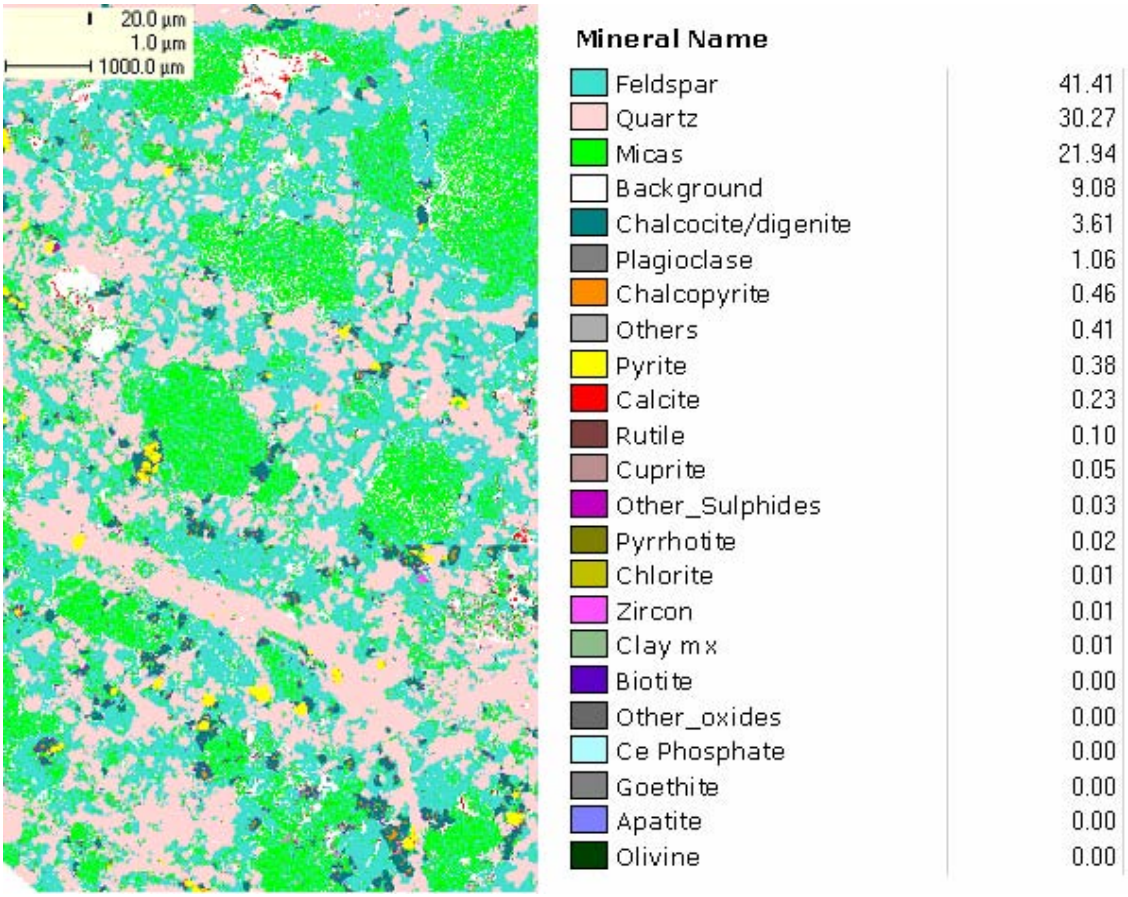

Figure 5.5. A representative QEMSCAN section of the sample #13

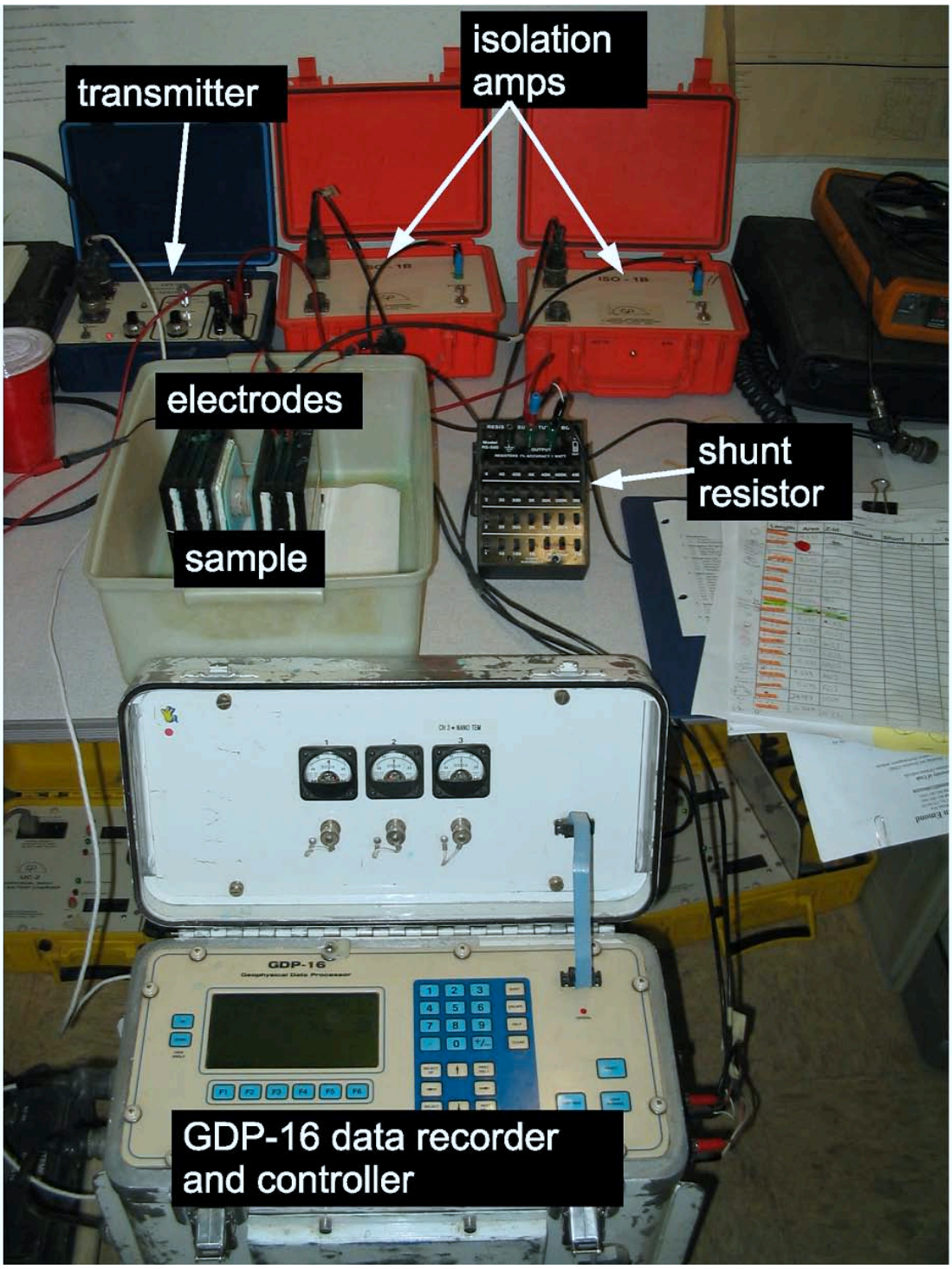

Figure 5.6. Recording system used at Zonge Engineering and Research Organization Inc. to obtain EM measurements.

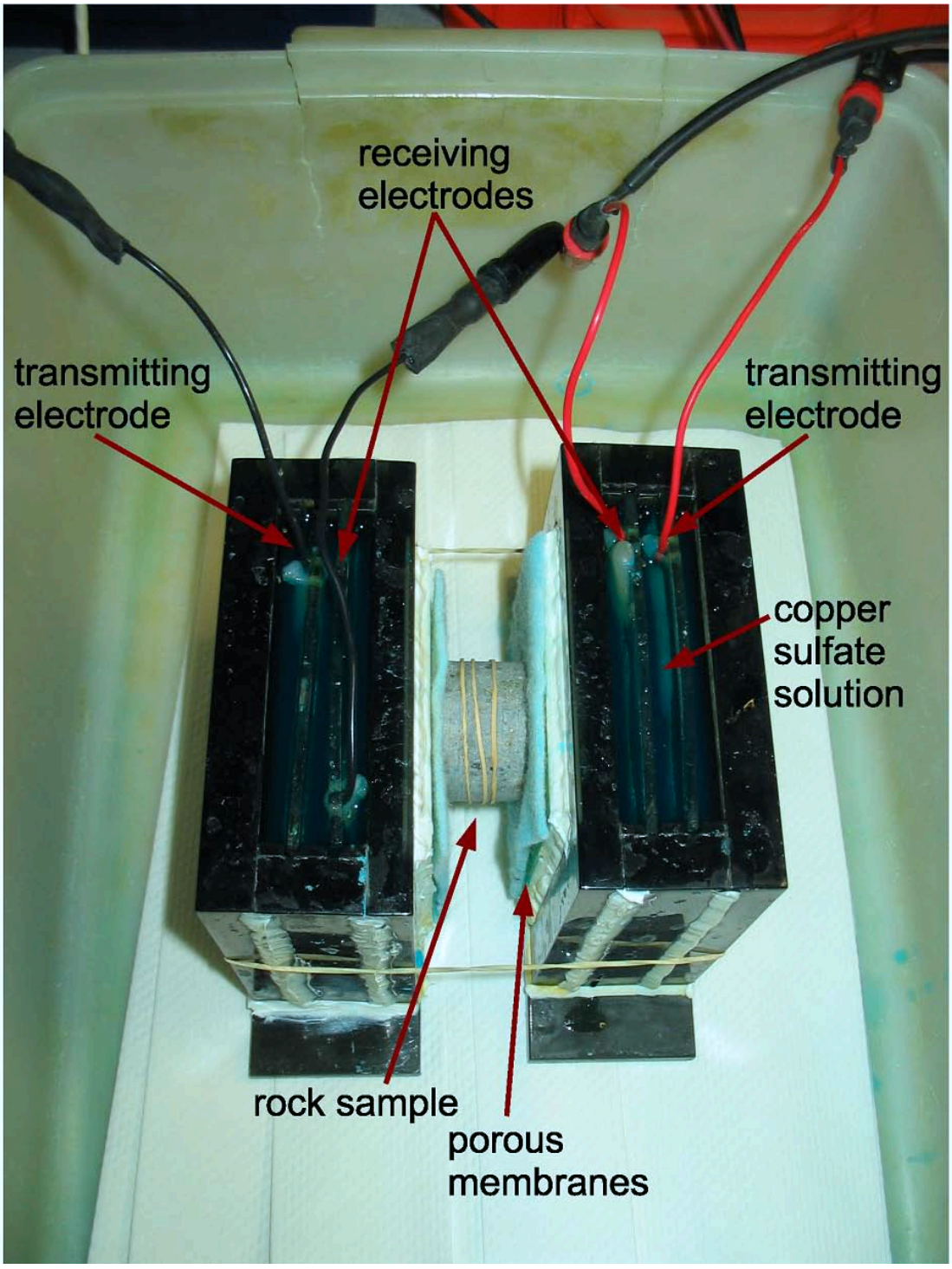

Figure 5.7. Sample holder, rock sample, and receiving and transmitting electrodes. Note the rubber band to prevent surface current flow across the rock sample surface.

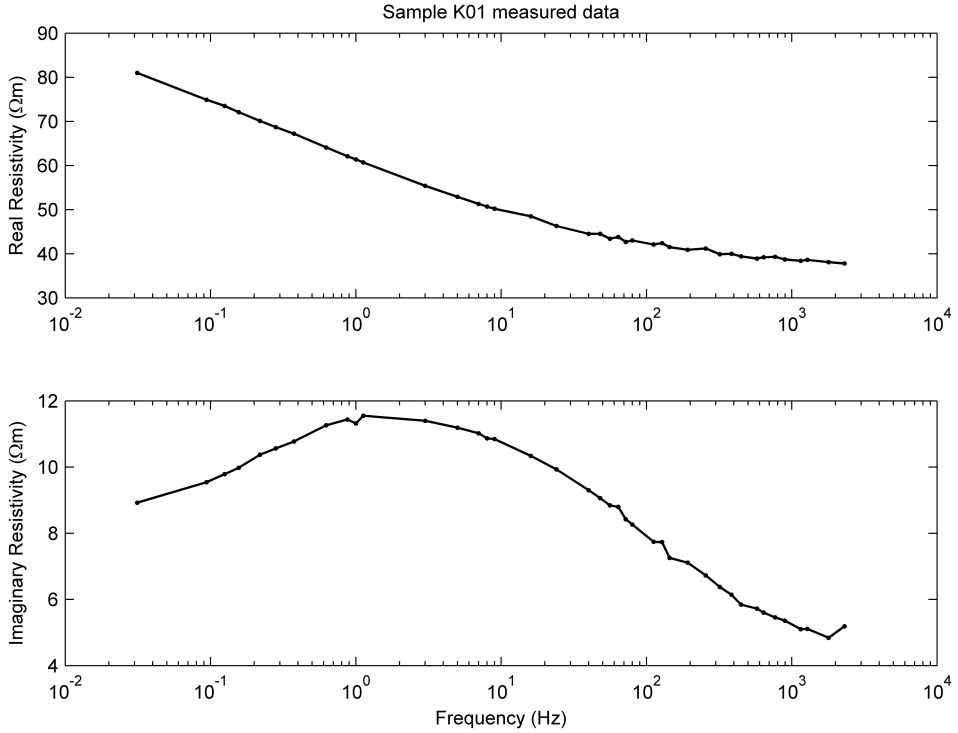

Figure 5.8. The plot of the resistivity data in the frequency domain for samples K01.

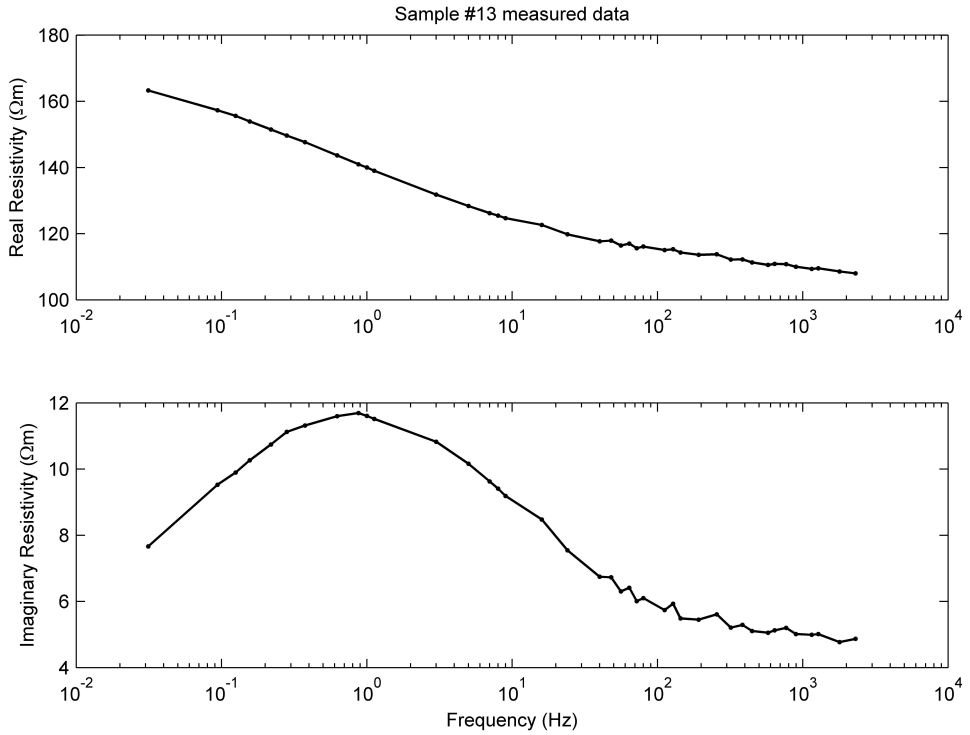

Figure 5.9. The plot of the resistivity data in the frequency domain for sample #13 in the first direction.

CHAPTER 6

INVERSION RESULT

This chapter discusses the inversion results based on the time-domain resistivity which is converted from frequency-domain resistivity by using the Fourier Transform. The routine based on the regularized conjugate-gradient (RGC) method (Zhdanov, 2002) was used for GEMTIP model inversion. As mentioned in Chapter 3, the RCG method, an iterative solver, updates the model parameters at each iteration using the conjugate-gradient directions.

Additional information about the samples was obtained by using the QEMSCAN and it was compared to the inversion results. In the case of the GEMTIP inversion, the recovered parameters are surface polarizability coefficient (α), the decay coefficient (C) and volume fraction (f). In the case of samples K01 and #13, the spherical GEMTIP model is used.

6.1 Sample K01

Sample K01 is a dacite from the Kori Kollo mine in Bolivia with disseminated pyrite and a predominantly sericite and quartz matrix. The diameter of the pyrite inclusions in this sample is $0.5 - 5mm$.

Figure 6.1 presents the plots of both the predicted and the measured time domain resistivity data and the misfit versus by iteration number. The resistivity is plotted over the time range from 10^{-3} to 1 second. Figure 6.2 presents the plot of the misfit functional in the model space formed by two parameters, α and C, for different iteration steps. After inversion, the surface polarizability (α) and decay coefficients (C) are determined. The final recovered values for α and C are 0.4 and 0.7.

Table 6.1 shows inversion parameters for sample K01 using the spherical GEMTIP model. The initial values for decay coefficients (C) and polarizability (α) are both 0.1.

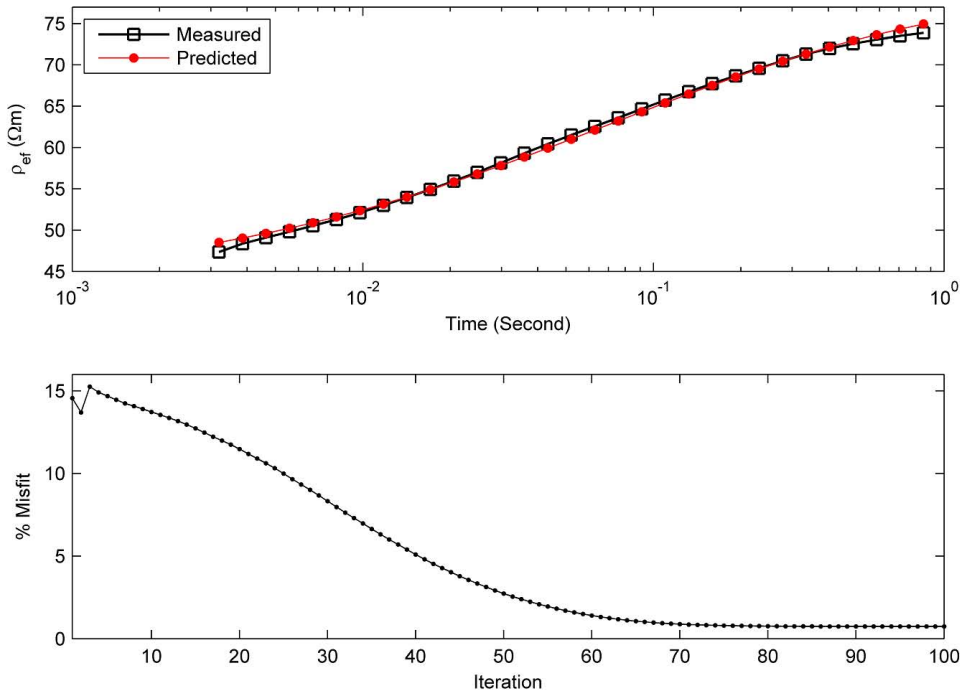

Figure 6.1. Sample K01: a) Measured and predicted effective resistivity curves plotted against time. b) Convergence of the misfit functional for a given number of iterations.

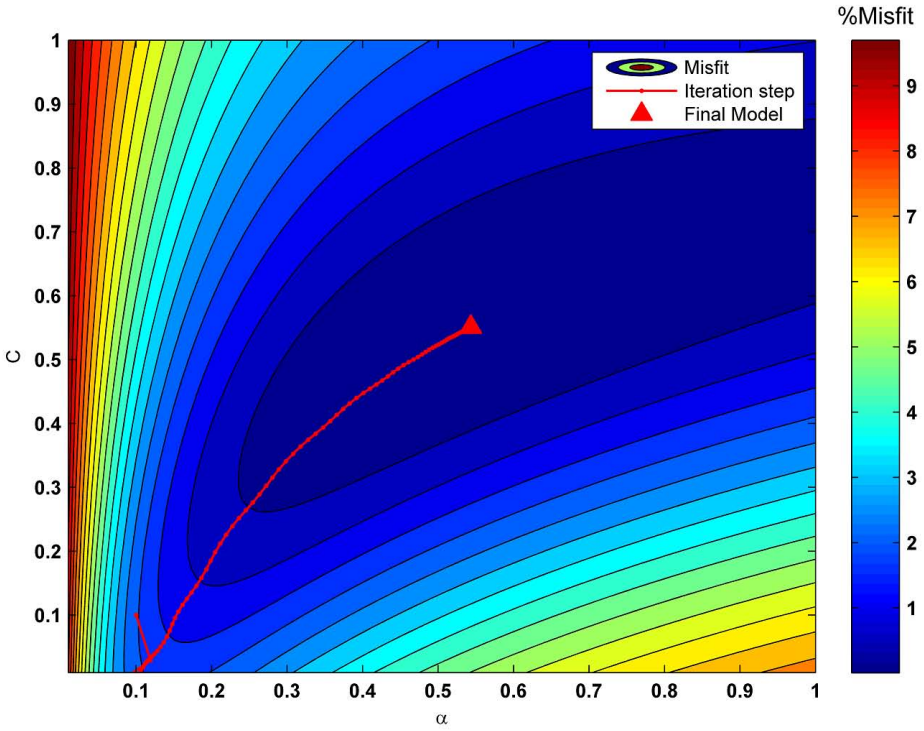

Figure 6.2. The misfit functional for sample K01, plotted with shaded isolines signifying the direction of decreasing misfit. The model steps are plotted using red solid dots. The final model is shown as a solid triangle.

Table 6.1. GEMTIP inversion parameters.

Variable	**Units**	**Initial**	**Recovered**
ρ_{matrix}	Ωm	81	-
f	-	0.07	-
C	Seconds	0.1	0.7
ρ_{phase1}	$\Omega\ m$	0.3	-
a	mm	2	-
α	$\frac{\Omega \cdot m^2}{sec^{c_l}}$	0.1	0.4

6.2 Sample #13

The rock sample #13 is from the Sar Cheshmeh Mine bench 2475 in Iran. This sample contains 3.6%Cu_2S (black dots). There is quartz in the veins.

Figure 6.3 presents the plot of both the predicted and the measured time domain resistivity data versus time, and the misfit as a function of the iteration number. The predicted data fit the measured data well. The resistivity is plotted over the time range from 10^{-3} to 1 second. Figure 6.4 presents the plots of the misfit functional in the model space formed by two parameters: surface polarizability (α) and decay coefficients (C).

The parameters of the spherical GEMTIP model for sample #13 are summarized in Table 6.2. By minimizing the Tikhonov parametric functional using the RCG method, the recovered value of the surface polarizability (α) equals 0.59, and the recovered value of decay coefficients (C) equals 0.47. The initial values for decay coefficients (C) and polarizability (α) are both 0.1.

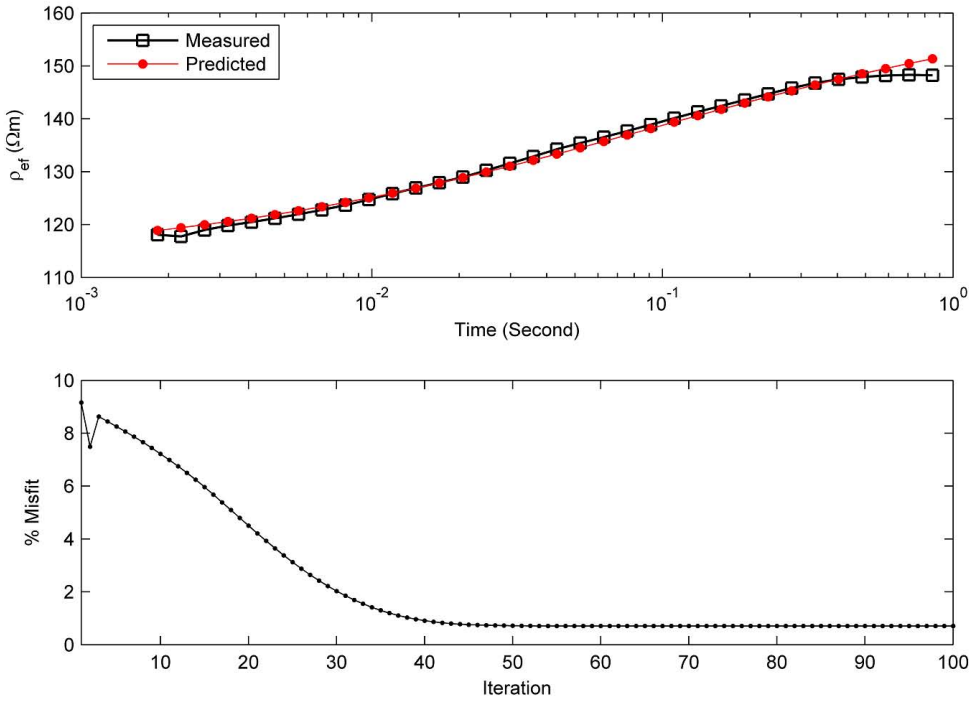

Figure 6.3. Sample #13: a) Measured and predicted effective resistivity plotted against time. b) Convergence of misfit functional for a given number of iterations.

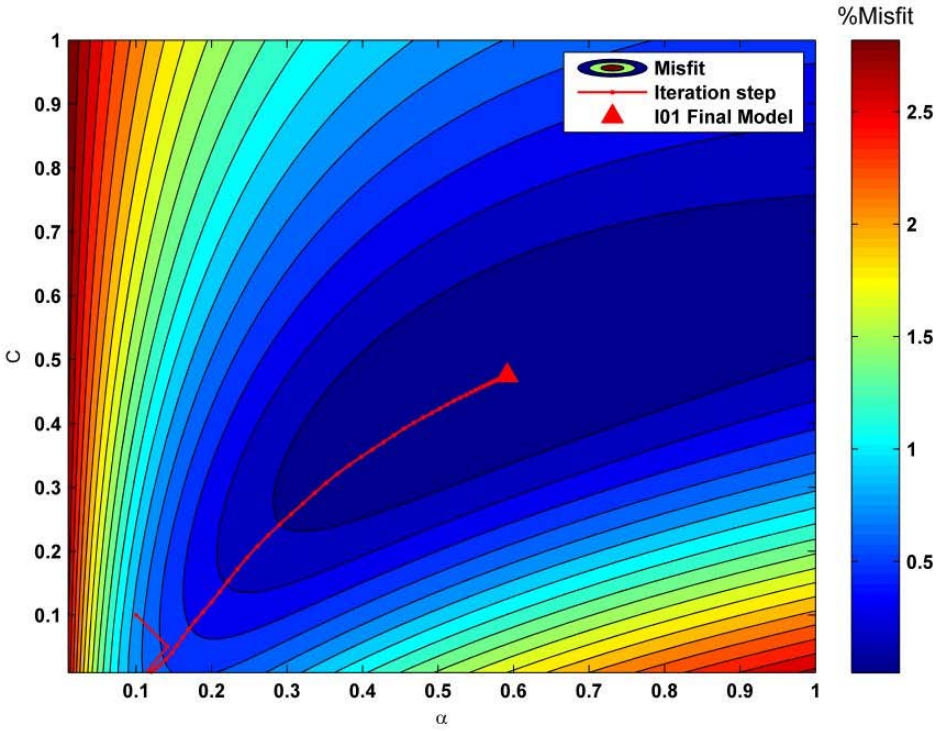

Figure 6.4. The misfit functional for sample #13, plotted with shaded isolines signifying the direction of decreasing misfit. The model steps are plotted using solid dots. And the final model shows as solid triangle.

Table 6.2. GEMTIP inversion parameters.

Variable	**Units**	**Initial**	**Recovered**
ρ_{matrix}	Ωm	163	-
f	-	0.05	-
C	Seconds	0.1	0.59
ρ_{phase1}	$\Omega\ m$	0.1	-
a	mm	2	-
α	$\frac{\Omega \cdot m^2}{sec^{c_l}}$	0.1	0.47

CHAPTER 7

CONCLUSIONS

I have evaluated the induced polarization effect in the time domain. Based on the transformation of the complex resistivity data from the frequency domain into the time domain data, it is shown that the IP effect in the time domain is different than the frequency domain. In the time domain, the IP effect is characterized by the change of the slope of the resistivity curve, as a function of time. It is demonstrated that the inversion results can be used as a mineral discrimination technique. Forward modeling has been done by using both the Cole-Cole model and GEMTIP model to study the IP effect in the time domain. The inversion result shows that the GEMTIP model is useful for understanding the composition of rocks.

Three porphyry system rock samples containing disseminated sulfides were measured to obtain the complex resistivity in the frequency domain. The frequency domain data were transformed into the time domain using a Fourier Transformation. This process was shown to provide useful information for GEMTIP model analysis of the rock samples.

In future the method can be tested on different types of rock samples. Further study may be done in testing the model with two or three different sulfide minerals. Additionally, more work should be done in application of the elliptical GEMTIP to study the influence of the ellipticity of the inclusions on the IP effect.

REFERENCES

[1] Emond, A.M., 2007, Electromagnetic Modeling of Porphyry systems from the Grain-size to the Deposit-scale Using the Generalized Effective Medium Theory of Induced Polarization: M.S. Thesis, University of Utah.

[2] Emond, A., M. S. Zhdanov, and E. U. Petersen, 2006, Electromagnetic modeling based on the rock physics description of the true complexity of rocks: Applications to porphyry copper deposits: 76th Annual International Meeting, SEG, Expanded Abstracts, 1313-1317a

[3] Flis, M. F., G. A. Newman, and G.W. Hohmann, 1989, Induced-polarization effects in time-domain electromagnetic measurements: Geophysics, **54**, 514-523.

[4] Frasier, D. C., 1964, Conductivity spectra of rocks from the Craigmont ore environment: Geophysics, **29**, 832-847.

[5] Hordt, A., T. Hanstein, M. Honig, and F. M. Neubauer, 2006, Efficient spectral IP-modeling in the time domain: Journal of Applied Geophysics, **59**, 152-161.

[6] Luo, Y., and G. Zhang, 1998, Theory and application of spectral induced polarization: Society of Exploration Geophysicists, Tulsa, OK.

[7] Ostrander, A. G., and K. L. Zonge, 1978, Complex resistivity measurements of sulfide-bearing synthetic rocks: 48th Annual International Meeting, SEG, Expanded Abstracts.

[8] Sumner, J. S., 1976, Principles of induced polarization for geophysical exploration: Elsevier.

[9] Zhdanov, M. S., 2002, Geophysical inverse theory and regularization problems: Elsevier.

[10] Zhdanov, M. S., V. Dmitriev, V. Burtman, A. Emond, and A. Gribenko, 2008, Anisotropy of induced polarization in the context of the generalized effective-medium theory: Proceedings of Annual Meeting of the Consortium for Electromagnetic Modeling and Inversion, 61-94.

[11] Zhdanov, M. S., 2008, Generalized effective-medium theory of induced polarization: Geophysics, **73**, F197-F211.

[12] Zhdanov, M. S., G. Keller, 2009, Geoelectrical methods in geophysical exploration: Elsevier.

[13] Zhdanov, M. S., V. I. Dmitriev, V. Burtman, A. Emond, and A. Gribenko, 2008, Anisotropy of induced polarization in the context of the generalized effective-medium theory: Proceedings of the Annual Meeting of the Consortium for Electromagnetic Modeling and Inversion, University of Utah, 61-94.

[14] Zonge, K. L., W. A. Sauck, and J. S. Sumner, 1971, Comparison of time, frequency, and phase measurements in induced polarization: Geophysical Prospecting, **20**, 626-648.

[15] Zonge, K., and J. C. Wynn, 1975, Recent advances and application in complex resistivity measurements: Geophysics, **40**, 851-864.